Brownian Motion of Magnetically Levitated Microsystems in Vacuum

By

Stephen Dunn

A thesis submitted to Macquarie University

for the degree of Master of Research

Department of Physics and Astronomy

January 2018

MACQUARIE
University
SYDNEY·AUSTRALIA

Examiner's Copy

Acknowledgements

I wish to acknowledge many of the people who have helped me to achieve so much this year, in not much of a particular order.

My many thanks to my supervisors Doctor James Downes, and Professor Jason Twamley, whose incredible creativity and grasp of the impossible made this fascinating project not only possible, but understandable and challenging. Your positive attitudes at all times made this journey manageable when the experiment when awry, or through the long hours of faceting. It has been a fantastic time working with you.

To Mattias Johnsson; thank you so much for your help in teaching me about the simulations, I couldn't have understood what I was doing without your help.

Thanks to Matthew O'Brien, for joining the team in the summer, helping move things along, and your lab skills - those you passed on to me, and those you didn't. We made some good progress because of what you did.

To my family - Carol, Rob, Mark, Ali, Katie, Craig - thank you all for your support this year, whether by just being fantastic people, or by keeping the due date a secret from Rob so he wouldn't stress out about it for me (even up until I'm writing this). Thanks for your support, and for showing an interest in my project, even though you might not know what on earth I'm talking about. But thank you most of all for putting up with me while I laze around, and don't contribute. Thank you for your patience with me in this, and for the nudges you give me for my betterment.

To all my friends at uni - Adam, Arv, Bryte, Connor, Ollie, Matt, Bron - thanks for making work survivable, by chilling out for an extra long lunch, or just by the constant physics memes. We may be new friends, but this year you have been as valuable to me as old school friends.

Thanks to Dale, my friend. Though we're busy, we make the time we can hang out worth every minute. You are a joy to have in my life, and I pray that our friendship will never fade.

To my girlfriend Caitlyn. Thank you for listening to me talk about this project. Thank you for putting in so much effort to understand what I was talking about. Thank you for being interested in it because I was interested in it. Thank you for the time with me you gave up so that I could get more work done. Thank you for being here for me. Thank you for your love. I love you.

Praise be to God, for I couldn't have completed this by my own strength, but only on His strength and power. Thank you for your blessings and the trials you give me. Thank you for everything.

And lastly, thank you to all the rest of the Physics and Astronomy Department. You are some of the most surprisingly friendly people I have ever met. Thank you for making the Department a place where anyone can be friends with anyone, and anyone can chat to anyone.

Abstract

This project aims to study the Brownian motion of a diamond micro-particle in a harmonic trap at pressures as low as 1×10^{-6} Torr. A novel, purely magnetic trap was designed with three dimensional magnetic modelling, optimising its shape to produce the highest resonant trapping frequencies. Experimental power spectral densities and mean square displacements match the theory very well, clearly showing observation of Brownian motion at low pressure. An attempt is also made to test the energy equipartition theorem at low pressure. There is potential for this trap configuration to be used to as a platform on which a macroscopic quantum superposition of states can be created and maintained one day. There is also more immediate potential of the miniaturisation and integration of this trap system into electronics as a precision inertial sensor.

Contents

1

Introduction

This project proposes the design and use of a novel magnetic trap to study Brownian motion at very low pressures, as a new possible trapping method for the creation of macroscopic quantum superposition of states, and for precision sensing technology. The study of Brownian motion at low pressures for the verification of Einstein's theory of Brownian motion is still largely unexplored. Firstly, we will discuss some of the history and fundamentals of Brownian motion relevant to this project. Then a slight detour will be made to explain the fundamentals of optical trapping, a technology which allows manipulation and observation of objects from the nano-scale to micro-scale, with focused lasers. This will become immediately relevant, as we will next outline recent optical trapping work which tested the energy equipartition theorem at low pressures by the observation of Brownian motion. After discovering the conditions that are necessary for the study of Brownian motion at low pressures, and how optical trapping meets them, we will outline the field of optomechanics, in which optical trapping has recently found a niche. This accommodation to the field of research focused on the study of the coupling of light with mechanical motion seems simple enough, but the fulfilment of the conditions for the study of Brownian motion are the same, though weaker, for the requirements in optomechanics

for creating a quantum superposition of states, and precision sensing technology. Thus, these goals become ultimate goals of the project. The penultimate section outlines the only other particle trap which traps using permanent magnets (to the author's knowledge). This is a good study to hold as a benchmark, as magnetic trapping of particles as harmonic oscillators is an emerging technology. Finally, the goals, and methods of our project shall be briefly outlined.

1.1 Brownian Motion

Brownian motion is the seemingly random movement of microscopic particles in fluid. It was first systematically documented by Robert Brown (after whom the motion is named), who observed the movement in micron-sized particles from organic and inorganic sources [1, 2]. Brown was satisfied by observation that the motion was not due to currents in the fluid, or evaporation. Almost 80 years later, after many attempts to explain the phenomenom, the first successfully convincing and rigourous explanation was given by Albert Einstein [3, 4]. Using kinetic atomic theory, Einstein showed that the random motions of the microscopic particles were exclusively caused by the thermal motion of the molecules making up the fluid. These molecules have insignificant kinetic energy in comparison to the inertia of the Brownian particle, but can produce the observed Brownian motion by constructive collisions; the collisions of molecules with the particle are random, but the net result for a set time is an extraordinarily large number of molecules pushing the Brownian particle in the same direction, resulting in the random changes in motion. The temperature and density of molecules in the fluid determines how rapid the change in the motion is, but the motion is always random. In explaining Brownian motion, Einstein derived the root mean square displacement of a Brownian particle,

$$\sqrt{\langle [\Delta x_{\text{dif}}(t)]^2 \rangle} = \sqrt{2Dt} = \sqrt{(2k_{\text{B}}T/\gamma)t}, \tag{1.1}$$

where $\Delta x_{\text{dif}}(t)$ is the displacement of a particle in the diffusive regime, D is the diffusion coefficient, k_B is the Boltzmann constant, T is the temperature of the fluid, γ is the Stokes friction coefficient, and t is time. This expression shows a dependence on the square root of time, a consequence of Brownian motion's characteristic random walk [5]. Furthermore, this expression was experimentally verified by Jean Perrin in 1909, the measurements shown in Figure 1.1. Perrin's work on Brownian motion was the primary reason he was awarded a Nobel Prize in 1926 [6, 7].

In a later paper, Einstein discussed the concept of the speed of a Brownian particle [4, 8]. By taking his expression for root mean square displacement and dividing by time, he gained an expression for the speed. However, this speed is shown to have an inverse square root relationship with time,
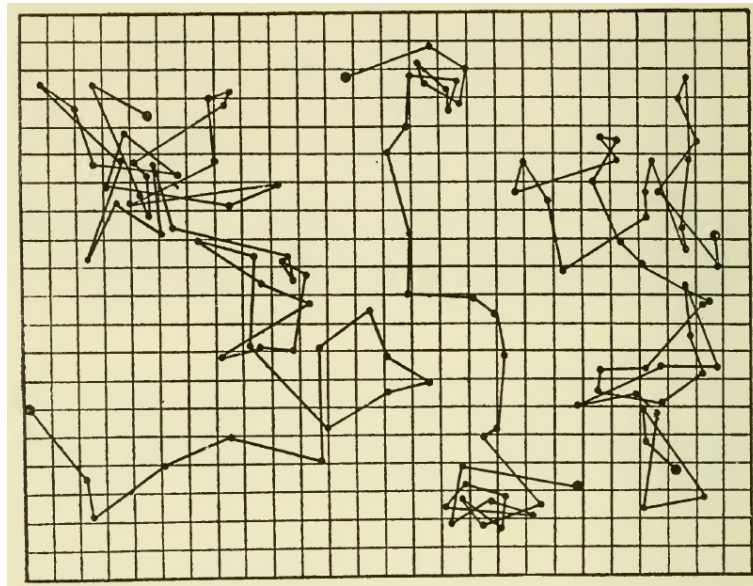
Figure 1.1: Perrin's experimental verification of Einstein's root mean square displacement formula. These measurements show the random nature of Brownian motion well [6, 7].

From Annales de Chimie et de Physique, Series 8, J. Perrin, Mouvement Brownien et Réalité Moléculaire, 1909.

resulting in non-physical speeds as time approaches zero. This led to the understanding that Brownian motion is continuous, but not differentiable. Einstein even went so far as to say that the concept of speed does not correspond to any physical property in terms of Brownian motion [5]. In that same paper, Einstein stipulated the equipartition theorem for Brownian particles, which states that "the kinetic energy of the motion of the centre of gravity of a particle is independent of the size and nature of the particle, and independent of the nature of its environment". If the instantaneous velocity of a Brownian particle were measured, then the kinetic energy of that particle could be calculated. As such, the energy equipartition theorem could be experimentally verified. However, as has been stated, Einstein did not think it was possible to measure the instantaneous velocity. This was mostly due to the limitations of the technology of the early 20th century, the time in which Einstein lived. On the other hand, this velocity can be measured with today's technology, and so the equipartition theorem of Brownian particles can be experimentally tested. A recent study did just that, using optical trapping in vacuum at low pressures. Firstly though, we will outline the general concept of optical trapping.

1.2   Optical Trapping

Optical trapping is a relatively recent technology, first reported by Arthur Ashkin *et al.* in 1986 [9]. It is the method of focusing a laser to hold, or trap, a microscopic particle. To understand how optical trapping works, we will consider the forces involved: the gradient, scattering, and gravitational forces. The gradient force is the trapping force, or restoring force. This force is dependent on the polarisability of the particle, which determines the degree to which applied electric fields from the laser generate dipoles in the particle. The resulting dipoles interact with the inhomogeneous electric field of the focused laser, resulting in a force in the direction of the field gradient [10]. For a focused laser with a Gaussian intensity profile, this force creates a three-dimensional potential well. This potential is harmonic for small excursions of the particle from the centre of the potential in any direction. The
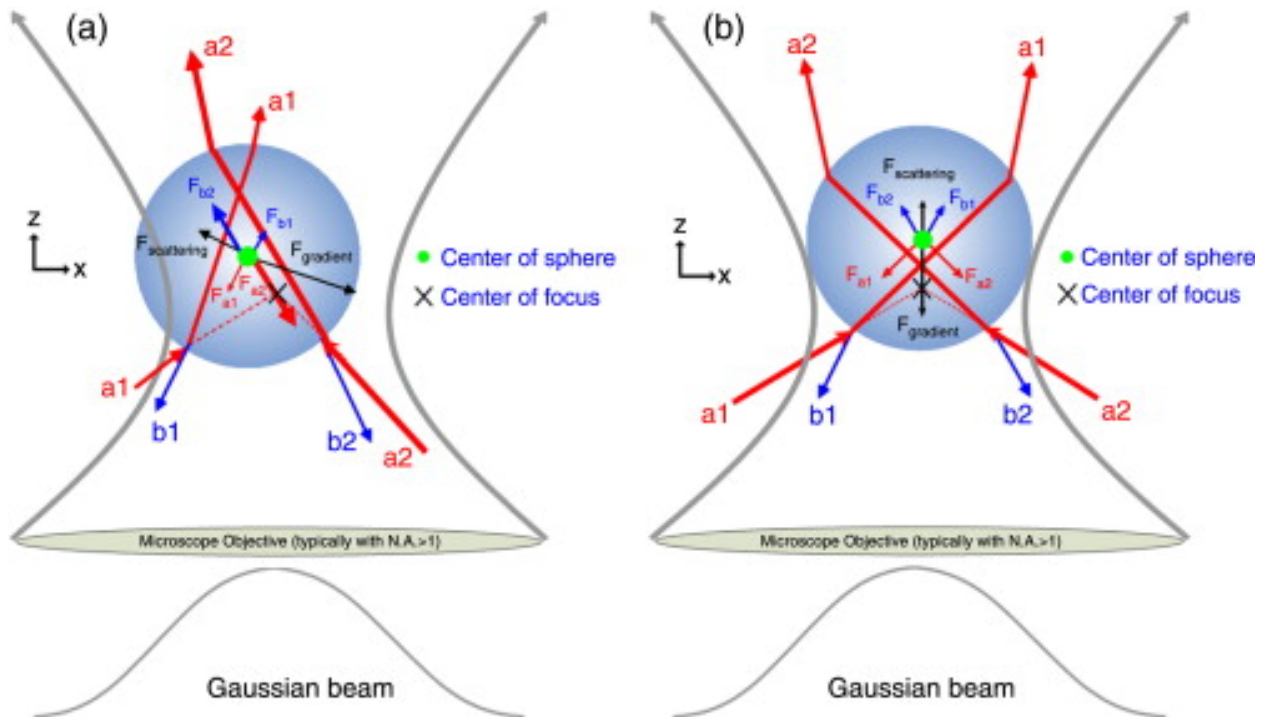

Figure 1.2: A ray optics description of the main forces involved in optical trapping for a Gaussian profile beam [11].

scattering force concerns the transfer of momentum from the absorption and re-emission of photons from the laser by the particle. The absorption of a photon results in a momentum transfer in the

direction that the photon was incident. There is also a momentum transfer due to the re-emission of photons. If this re-emission is an isotropic process, then the net momentum transfers from re-emitted photons will average to zero after many re-emissions. Thus the particle experiences an average force in the direction of the incident photon due to the momentum transfer associated with the absorption of photons. The net result of this force is to shift the potential well from the focal point in the direction of the propagation of the beam. The gravitational force simply applies a force on the particle downwards, shifting the potential well downwards. As a result of the gravitational and scattering forces, the centre of the potential well is below and along the beamline from the focal point. Optical trapping developed the capability to isolate, manipulate and monitor an individual particle in water, but particles have also been optically trapped in air and vacuum successfully [9, 12]. An example of this was the study in which Brownian motion and the energy equipartition theorem were tested at low pressures [12].

1.3   Brownian Motion in an Optical Trap

While Einstein thought that the instantaneous velocity of a Brownian particle was practically impossible to measure, a recent study reported measuring this variable by using optical trapping, and fast photodetectors [4, 8, 12]. The Brownian motion that Einstein described was in the regime where the observation time scale is much larger than the time it takes a Brownian particle to be stopped by the thermal motion of the fluid molecules, called the momentum stopping time τ_p. This is to say that the regime in which Einstein explained Brownian motion was that where the observations took place many times less frequently than the change in direction of the Brownian particle. This regime is the diffusion regime, defined by $t >> \tau_p = m/\gamma$, where m is the mass of the Brownian particle, and γ is the Stokes friction coefficient of the fluid environment. However, for time scales much shorter than τ_p, the Brownian motion is in the ballistic regime, such that the true motion of the Brownian particle can be measured.

In this regime, Einstein's diffusive results for the mean square displacement (MSD),

$$\langle [\Delta x(t)]^2 \rangle = 2Dt = (2k_BT/\gamma)t, \tag{1.2}$$

do not describe the motion of a Brownian particle. Instead, the motion is dominated by inertia, and the MSD is given by

$$\langle [\Delta x_{\mathrm{bal}}(t)]^2 \rangle = (k_BT/m)t^2 = (D/\tau_p)t^2, \tag{1.3}$$

obtained from the Langevin equation, where $\Delta x_{\mathrm{bal}}(t)$ is the displacement of a Brownian particle in the ballistic regime, and is dependent on t^2. This means that, though there is no meaning for an

instantaneous velocity of a Brownian particle in the diffusive regime, an instantaneous velocity of a Brownian particle exists in the ballistic regime. In this study, the momentum relaxation time of a Brownian particle was increased by decreasing the density of the air by decreasing the pressure in the vacuum chamber to as low as 2.75 kPa. This decreased the Stokes friction coefficient, and allowed the observation time scale to become much less than τ_p. An optical trap was used to suspend the Brownian particle in air, while also enabling observation of the suspended particle by producing an image of that particle. The trapped particle in this study was a micron sized spherical silica bead. The optical trap consisted of 2 counter-propagating lasers which optically trapped the bead in the vacuum chamber, causing the average scattering forces to cancel. To avoid interference signals, the lasers were orthogonally polarised and detuned in frequency. The image from one beam was bisected by a sharp D-mirror, dividing the image, with each half collected by a fast photodiode detector. The resulting signal was related to the position of the particle in one dimension. Position measurements as a function of time were made at 99.8 kPa and 2.75 kPa. The finite difference method was used on the position measurements to find the instantaneous velocity. The normalised velocity distribution at each pressure was plotted, and found to match the normalised Maxwell-Boltzmann distribution for room temperature,

$$f(v) = \exp\left(-\frac{mv^2}{2k_\mathrm{B}T}\right), \tag{1.4}$$

regardless of the change in pressure, where v is the instantaneous velocity of the Brownian particle. As stated above, the energy equipartition theorem states that the kinetic energy of the motion of the centre of gravity of a particle is independent of the shape and nature of the particle, and of the nature of the environment, and that the average energy of a particle will be distributed equally among available degrees of freedom. Thus, for a particle in thermal equilibrium with room temperature, the root mean square velocity can be calculated. The measured root mean square velocities were within the uncertainty (about 5%) of the prediction of the equipartition theorem, which was within the noise of the measurements. This confirmed the energy equipartition theorem down to these pressures. Measured values were used to fit curves to the data for measured mean square displacements, which matched the theory from the Langevin equation, [13]

$$\langle[\Delta x_\mathrm{tra}(t)]^2\rangle = \frac{2k_\mathrm{B}T}{m\omega_0^2}\left[1 - \exp(-t/2\tau_\mathrm{p})\left(\cos(\omega_1 t) + \frac{\sin(\omega_1 t)}{2\omega_1\tau_\mathrm{p}}\right)\right], \tag{1.5}$$

where $\Delta x_\mathrm{tra}(t)$ is the displacement of a trapped particle in the ballistic regime, ω_0 is the resonant frequency of an undamped trapped particle, and $\omega_1 = \sqrt{\omega_0^2 - 1/(2\tau_p)^2}$. Figure 1.3 clearly shows the difference of Einstein's predictions for the diffusive regime and the results for the ballistic regime.

The measured MSDs show close agreement with the theory at short time scales. At long timescales,
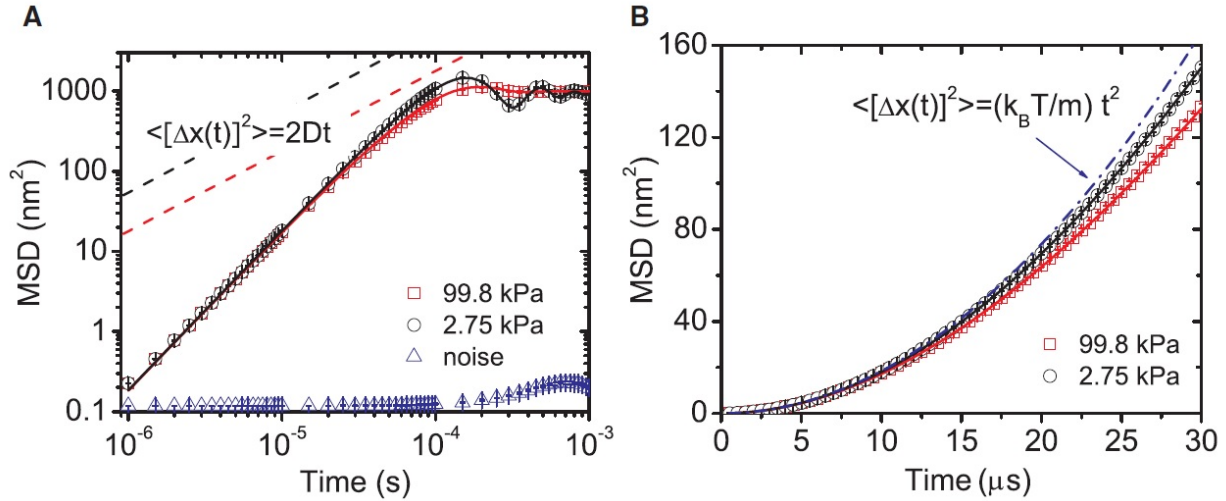

Figure 1.3: MSDs from the study of Brownian motion at low pressure using an optical trap. The symbols are the experimental data. A) The experimental MSDs clearly show ballistic Brownian motion, by the agreement with the theory (solid red and black lines, given by Equation 1.5), and disagreement with the diffusive theory (dashed lines, given by Equation 1.2). The oscillation and convergence to a constant is due to the trapping. B) The experimental data has a clear t^2 dependence. The dotted line is the theory for a free Brownian particle in the ballistic regime [12].

From Science, Vol. 328, Issue 5986, T. Li, S. Kheifets, D. Medellin, M. G. Raizen, Measurement of the Instantaneous Velocity of a Brownian Particle, pp. 1673-1675, Copyright (2010). Reprinted with permission from AAAS.

the mean square displacement converges to a constant value due to the optical trap. Thus, the equipartition theorem and Maxwell-Boltzmann velocity distribution were experimentally confirmed, and the instantaneous velocity of a Brownian particle was observed. However, the conditions under which the equipartition theorem was tested here were limited, likely due to the balance of trap strength, laser heating and cooling necessary to optically trap at lower pressures. As such, further testing of the equipartition function could be done at lower pressures, with a trap that does not intrinsically heat the motion of the trapped particle, as will be done in this project. The conditions necessary for the observation of the instantaneous velocity of a Brownian particle - a harmonic oscillator, and reduced damping from the environment - are similar to those necessary in reaching the goals of optomechanics.

1.4   Optomechanics

The field of optomechanics studies the effect of radiation pressure on mechanical systems, such as the mirrors of interferometers. To study these effects with high sensitivity, high mechanical quality harmonic oscillators must be developed. As a result of developing such sensitive oscillators with low noise environments, high precision sensing technology can be developed. This technology uses these sensitive oscillators to measure things like changes in inertia, or electromagnetic waves. Precision sensing technology is such a big application of optomechanics research that it has become a secondary goal of the field [14].

The archetypical optomechanical system is an optical cavity formed by one fixed mirror, and another mirror on a cantilever, such that the cantilever allows that mirror freedom to move in one dimension [15]. This freedom of movement allows for the radiation pressure from a laser to change the length of the cavity, and hence change the resonant frequency. This can be exploited to cool the motion of the mirror by detuning the laser frequency below the natural cavity resonant frequency. Cooling of the motion of the mechanical oscillator to the motional ground state is necessary to comprehensively study the coupling of light with the mechanical motion. Typical optomechanical setups are affected by mechanical noise through contact of the cavity mirrors with the environment, limiting the ability to cool the motion of the oscillator. More recently, optical trapping of the oscillator in vacuum has been used to reduce the environmental mechanical noise by isolating the mechanical oscillator from the mechanical environment [16]. The motion of an optically trapped mechanical oscillator can be cooled by the use of active feedback cooling from an additional laser beam in each direction, and has been achieved to the millikelvin regime [17]. By measuring the position of the oscillator, its instantaneous velocity can be calculated, as above. The intensities of the cooling beams are then modulated to apply a force proportional to that velocity, opposing the motion, such that the oscillator is forced to the centre of the trap. Cooling can be made even more efficient by isolating the oscillator from sources of thermal noise. This isolation and the cooling to the motional ground state are necessary conditions for the creation of a long-lived, macroscopic, quantum superposition of states, or cat state, after Schrödinger's cat thought experiment. As these conditions align with the conditions of studying the coupling of radiation pressure with mechanical systems with high sensitivity, it became one of the goals of optomechanics to create cat states [14].

The cat state is sensitive to noise from the environment, which destroys the quantum effects by decoherence, returning the state of the oscillator to the classical physics regime. Therefore, the oscillator must be isolated from the sources of decoherence for the cat state to be maintained. This

isolation from noise includes the collisions from the thermal motion of a gas environment, which can be reduced by decreasing the pressure of the environment. It has been proposed that diamond nano-particles with nitrogen vacancy centres could be optically levitated, as the vacancy centre provides a quantum handle on the cat state [18]. However, it has been found that optically trapped nano-diamond burns and graphetises at low pressure, setting back this proposal with optical traps [19]. However, this proposal could still be achieved by using a trap which doesn't intrinsically heat the trapped particle. A recent study has done just this, using a magneto-gravitational trap to levitate diamond nano-crystals with nitrogen vacancy centres, and measure the excitement of the flouresence of those NV centres at high vacuum pressures without burning or graphitising the diamond [20].

1.5   Magneto-Gravitational Trap

A recent study was published involving a trap with limited intrinsic motional heating of the trapped particle [20]. Light is not used for the trapping mechanism in this study; instead, magnetic and gravitational forces are used to trap a particle. In order for stable magnetic trapping to be achieved, a diamagnetic material must be involved [21, 22]. The simplest arrangement is when the particle to be trapped is diamagnetic. This particle will experience a force in an inhomogeneous magnetic field away from the increasing field gradient, as shown by the equation of the magnetic force

$$F_{\text{mag}} = \frac{\chi V}{2\mu_0} \nabla B^2 = \frac{\chi V}{\mu_0} B \nabla B, \tag{1.6}$$

where χ is the magnetic susceptibility of the particle, V is the volume of the particle, μ_0 is the permeability of free space, and $B = (\mathbf{B} \bullet \mathbf{B})^{1/2}$ is the magnitude of the magnetic field vector $\mathbf{B}$. Thus, the strength of the magnetic force on a diamagnetic particle depends on both the local magnetic field strength, and the local magnetic field gradient. As such, a diamagnet will seek a lower magnetic field to minimise its energy. In this recent study, the magnetic field was engineered using 2 anti-parallel permanent magnets, as seen in Figure 1.4a. FeCo pole pieces were shaped to concentrate the magnetic field in the small region shown in the centre of Figure 1.4b. This region was where the trapping potential was formed. The shape of the pole pieces in Figure 1.4, with shorter z dimensions for the upper pair than the lower pair, created an upward curved potential well along the z-axis. The force due to gravity prevented the particle from exploring the full length of this curved potential trough and escaping. Thus, the trap relied on gravity to trap in the z direction, and magnetic fields to trap in the x and y directions. In the study, diamond nano-crystal clusters were trapped under vacuum [20]. These diamond nano-crystals contained nitrogen vacancy (NV) centres, as described in the proposal
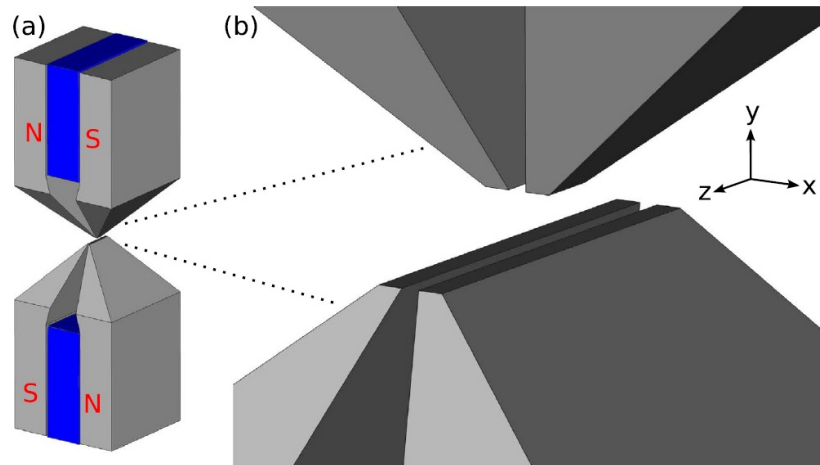
Figure 1.4: (a) The arrangement of the rare earth magnets (blue) and FeCo pole pieces (grey) used to create the trapping potential in the magneto-gravitational trap. (b) An enlarged view of the trapping region. Note that the upper pole pieces are not the same dimensions as the lower pole pieces, creating a magnetic potential which curves gently upward from the centre along the z direction, such that gravity is required to form a trapping potential [20].

From Sci. Rep., Vol. 6, Article 30125, J.-F. Hsu, P. Ji, C. W. Lewandowski, B. D'Urso, Cooling the Motion of Diamond Nanocrystals in a Magneto-Gravitational Trap in High Vacuum, Copyright (2016) Springer Nature. Reused under Creative Commons License CC BY, with the only modifications being exclusions of the original caption and part c of the figure.

above. The fluorescence of the zero phonon line of these NV centres was used to confirm the identity of the trapped particles, and to show that the fluorescence could be measured with the setup of this trap without losing the diamonds. In order to characterise the trap, the resonant frequency of each mode was found by tracking the motion of a trapped diamond nano-crystal cluster and producing the power spectral densities (PSDs). Theoretical calculations give the resonant frequencies as 104 Hz, 130 Hz, 9.6 Hz for the x, y, and z modes, respectively. To observe these frequencies experimentally, diamond nano-crystals were loaded, which formed a cluster once trapped. A 520 nm laser drove the fluorescence of the NV centres, and an 830 nm laser was used to detect the motion of the cluster. Light scattered from the cluster was collected and directed to a high speed camera, and quadrant photodiode detector. The high speed camera was used to track the centre of mass motion of the cluster, producing the position measurements for the PSDs. The peaks of these plots show the oscillation frequency of the trap in each measured direction. Lower pressures have less damping, and so showed taller, thinner peaks in the PSD. The ratio of the height to width of these peaks provides a measure for the

mechanical quality factor (Q_{mech} factor) of the trap at different pressures. The Q_{mech} factor indicates how long the cluster takes to lose energy to the environment, so is ideally maximised. To reduce the possibility of heating the motion of the diamond with the lasers, only low power lasers were used, and the 520 nm laser was pulsed to allow time for cooling of the additional energy. Direct feedback cooling was implemented by a current carrying wire, which runs over the lower pole pieces, out of the trapping region. The current produces a magnetic field, providing another magnetic force upon the diamond. The position signal measured by the quadrant photodiode was used to find the displacement from the centre of the trap in each direction. This displacement was used to determine the amplitude of each direction's cooling signal. These cooling signals were driven at the corresponding resonant frequency of the trap. As the resonant frequencies of the trap were well separated, each of these signals only significantly affected the motion in the desired mode. These cooling signals were then filtered, amplified, phase shifted, and combined to produce the total cooling signal. With this setup, the research group was able to keep a diamond nano-crystal cluster trapped at 7×10^{-8} mbar because of the cooling system.

This passive trap gives impressive results. However, the trap relies on gravity for trapping in its final dimension, limiting the applications of this technique in the future, as the trap must be kept upright at all times. Additionally, the resonant frequencies are relatively small, especially compared to the frequencies achievable with optical trapping - in the kilo-Hertz regime [17]. Indeed, the researchers admitted their trap was "soft", though claimed that this was key to its success.

1.6   Magnetic Trap

This project proposes a fully magnetic, passive trapping technique. This technique does not intrinsically inject energy into the oscillator system by the trapping mechanism. The capability of this fully magnetic trap to keep a particle trapped will not rely on the change in potential due to gravity, and will be designed to be a strong trap with high resonant frequencies, unlike the magneto-gravitational trap. To ensure this, the trap will be optimised by modelling the magnetic field in three dimensions. Particle kinetics will be simulated for this optimised magnetic trap, using a Langevin equation and a numeric differential solver, with these PSDs and MSDs compared to the theory to test the effectiveness of the simulations. The modelling can only be tested by the experimental results. This trap will be used to test the equipartition theorem at conditions far more extreme than previous optical trapping experiments (at pressures reaching 1×10^{-6} Torr), and to observe the individual Brownian motion effects at these

extreme conditions. This will be done by finding the velocity distributions, the MSDs, and calculating the root mean square velocity, as in the previous Brownian motion study [12]. The PSDs will also be plotted, which also show the Brownian motion, but are primarily useful for identifying the power of the resonant modes, and identifying the resonant frequencies and cooling temperatures, as in the magneto-gravitational study.

2

Modelling

In this chapter we will discuss the feasibility of a purely magnetic trap, and how the magnetic trap can be engineered by choosing magnet shapes. Furthermore, our ideal magnetic trap will be modelled, plotting the resonant frequency for diamond micro-particle for varying shape parameters. The movement of a trapped diamond micro-particle will be simulated, analysed, and compared to the Brownian theory.

2.1   Magnetic Trapping for One Dimension

In this section we will outline the theory of a purely magnetic trap, using finite element modelling to prove that the concept of trapping a micron-scale diamagnetic particle with permanent magnets in one dimension is theoretically possible.

In Chapter 1 it was seen that trapping diamond particles has been achieved with a permanent magnet based magneto-gravitational trap. This trap requires no power - electrical, optical, or any other external energy injection - in order to trap, which is beneficial for later integration into electronics as a precision

sensor. However, the magneto-gravitational trap is reliant on orientation, as gravity is a key in forming the trapping potential. This limits the application of this trap in electronics. Furthermore, this trap has very low resonant frequencies, whereas the creation of a macroscopic quantum superposition of states requires a high resonant frequency. This relation can be seen through the mechanical quality factor, Q_{mech}, which must be maximised for quantum applications, and depends on the resonant frequency by $Q_{\text{mech}} = \omega_j/\Gamma_0$, where ω_j is the angular resonant frequency in the j dimension, and Γ_0 is the damping coefficient. This leaves little application for the current magneto-gravitational trap design. On the other hand, we believe a strong, fully magnetic trap will have great potential to meet both of these goals. Therefore, we endeavour to design a trap which has high resonant frequencies, can trap diamond micro-particles at low pressures, all without requiring any form of power to keep a particle trapped.

With this aim in mind, our design goal is to engineer the magnetic field between two powerful rare-earth magnets, such that a local magnetic field minimum surrounded by a strong field gradient is produced. This will be achieved by choosing an appropriate shape for the magnets. If we are able to design the magnetic field effectively, our trap will have a strong trapping potential, as given by

$$U_{\text{mag}} = -\frac{\chi B^2 V}{2\mu_0}, \tag{2.1}$$

. Note that χ is negative for a diamagnetic material, such that a diamagnetic particle will seek a magnetic field minimum to minimise its energy. We find the force on the particle from this potential to be $F = -\nabla U = (\chi V/\mu_0)B\nabla B$, as in Equation 1.6. Therefore, to produce the greatest trapping force, we must have a strongly increasing magnetic field gradient, such that both ∇B and B will be maximised. Our chosen configuration has the like poles of two rare-earth magnets facing each other. This will result in the repulsion of the magnetic fields from each magnet, forming a magnetic field minimum. We used finite element analysis modelling (the program FEMM) to model the magnetic field of cylindrical magnets with conical shaped tips. The conical shaped tip encourages the magnetic field to flow through the magnetic material to the tip vertex, rather than leaving the magnet earlier due to the presence of the opposing magnetic field. As such, the magnetic field which comes from the tip vertex is very strong, creating the desired trapping environment.

To test the ability of this setup to trap diamagnetic material, values were taken from the FEMM model in order to perform a calculation of the resonant frequency of the axial mode. Instead of diamond, we will use graphite in this rough calculation, as we wish only to prove that our design concept is feasible, and graphite is more strongly diamagnetic than diamond, and less dense. The modelled magnets were 8 mm long, with a radius of 1 mm, with conical tips with an angle of ascension

from the base of the cone to the side of the cone of $45°$, similar to what is shown in Figure 2.5. The gap between the tip vertices was set as 100 μm. The measurements from the FEMM modelling are displayed in Figure 2.1. Figure 2.1a shows the magnetic field along the axial axis in the gap between the magnet tips. This shows a promising shape, with the field reaching 0 T at the centre of the gap, producing a minimum in the potential. Figure 2.1b gives a clearer indication of the approximately linear, central region in Figure 2.1a. This region should produce a harmonic potential. By taking the values of the magnetic field at 0.02 mm and 0.06 mm as 0.2 T and -0.2 T respectively, we find the linear equation which approximates the magnetic field in the region near the centre of the trap. Using this equation for the magnetic field, we can calculate the acceleration of a graphite particle due to the magnetic field, using $\chi_{\text{gra}}/\rho_{\text{gra}} = -2.0 \times 10^{-7}$ m^{3}kg^{-1} for graphite, where χ_{gra} is the magnetic susceptibility of graphite, and ρ_{gra} is the mass density of graphite [23]. Examining the equation for the acceleration of a harmonic oscillator

$$a = -kx/m = \omega_0^2 x, \tag{2.2}$$

where k is the spring constant, x is the position of the oscillator, and m is the mass of the oscillator, we see that we can find the resonant frequency by taking the spatial derivative of the acceleration. Thus, as $\omega_0 = 2\pi\nu$, we find the linear resonant frequency of the magnetic trap, ν, with conical tips in the axial dimension as approximately 600 Hz. This resonant frequency is already much higher than the highest resonant frequency in the magneto-gravitational trap, prior to any optimisation of our design, indicating that our pure magnetic trap has the potential to work. However, it should be noted that the magnetic susceptibility of graphite is anisotropic, with the value used above being true in only one dimension; in the other dimensions, the susceptibility is weaker. In the other dimensions, the resonant frequency would be around 200 Hz. Therefore, the case shown above only demonstrates the proof-of-concept for the basic idea of our design - that it has some potential to be proven successful.

In this section we have proposed the design of a purely magnetic trap. The theory of magnetic trapping was reviewed, and the suggested magnet tip shape outlined. Modelling with finite element analysis software gave the magnetic field between 2 cylindrical magnets with conical tips with angle of ascension of $45°$. This field was used to calculate the resonant frequency in the axial direction as roughly 200 Hz, suggesting our magnetic trap design has the potential to be an effective trapping method.

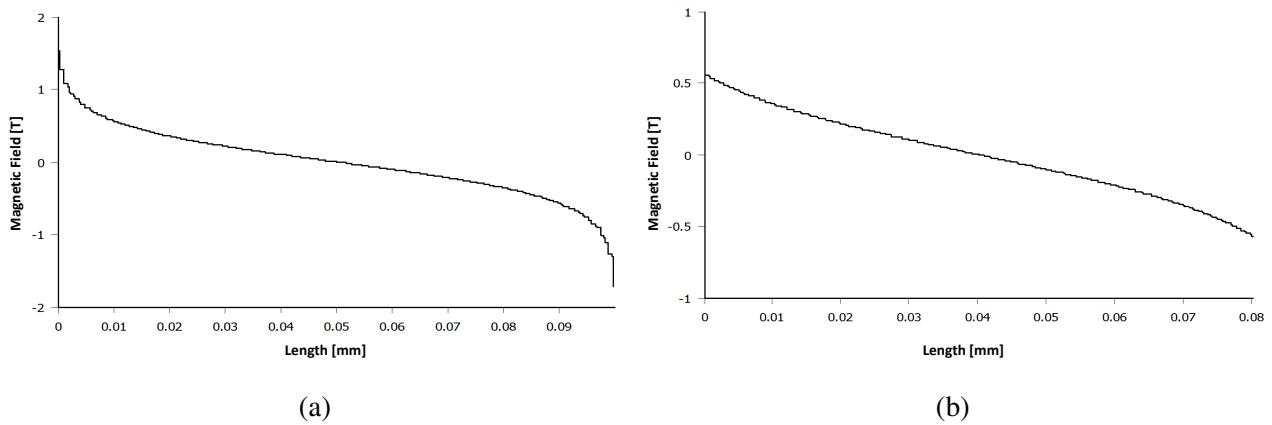(a)   (b)

Figure 2.1: The magnetic field as modelled by the FEMM program along the axial axis, between 2 cylindrical magnets with 45° conical tips, and a gap between the tips of 100 μm. (a) The magnetic field in the axial direction from magnet tip to magnet tip. (b) The magnetic field in the axial direction, focused on the approximately linear, central region from (a), such that 0 mm in (b) is at 0.01 mm on (a). This region provides an approximately harmonic potential, with a resonant frequency of 600 Hz for a graphite particle.

2.2 Modelling of a Magnetic Trap in Three Dimensions

In the previous section, simple modelling was produced to prove that the concept of a purely magnetic passive trap was possible. In this section, three dimensional modelling shall be shown to optimise the design of the magnetic trap, such that it is capable of trapping diamond micro-particles.

It is necessary to optimise the shape of our magnets to create a strong potential, so that a diamond micro-particle will be strongly trapped at low pressures. Using a 3D modelling package for Mathematica called Radia, we modelled the conical tip trap introduced above in three dimensions [24]. However, as the magnetic trap is axially symmetric, we need only consider the magnetic field in two dimensions: the axial and radial dimensions. We modelled the magnets with the same length and radius as the magnets in the FEMM simulation (8mm and 1mm, respectively), varying the angle of ascension of the cone tip, and gap size. The magnetic material modelled was a NdFeB magnet, with an internal field of 1.2 T. Note that the magnetic field is weaker in the radial dimension than in the axial dimension, the resonant frequencies for the radial mode will be lower. In calculating the resonant frequencies we used a $\chi_{\text{dia}}/\rho_{\text{dia}}$ of diamond equal to -7×10^{-9} m^{3}kg^{-1} [25]. Calculating the resonant frequencies of the two modes separately, we plot as a function of gap size and angle of ascension, and assuming an harmonic potential near at the centre of the trap. These results are displayed in Figures 2.2a and 2.2b for the axial and radial dimensions, respectively. These plots show that the

smaller the gap between magnet tips, the higher the resonant frequency. However, the trend shown is not likely to be entirely accurate at small gap sizes, due to the strong repulsion from the like poles of the magnets. This will result in the demagnetisation of some of the magnetic material, reducing the resonant frequency, which is not considered by this model. Examining Figures 2.2a and 2.2b also reveals that there is an optimal angle of ascension for maximising the resonant frequency around 35°.

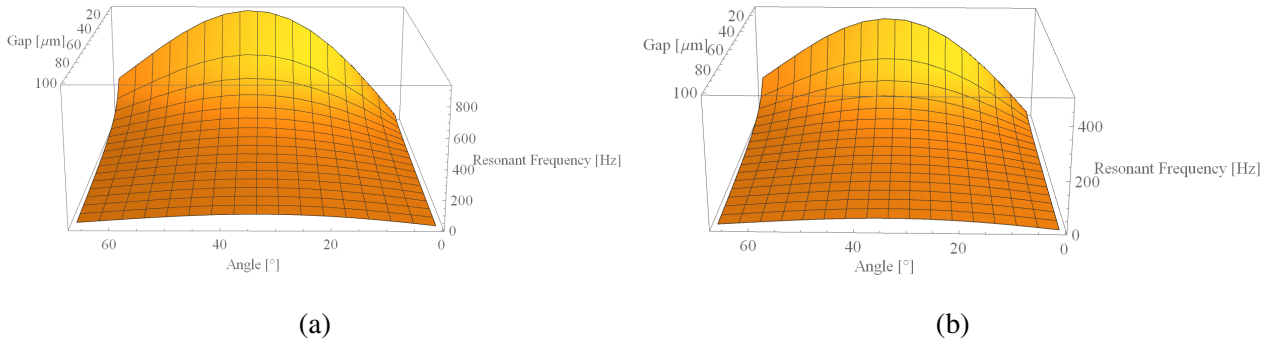(a)   (b)

Figure 2.2: Resonant frequency for diamond micro-particle in the (a) axial and (b) radial modes, for a conical tip magnetic trap, as a function of gap size and angle of tip ascension. The angle that gives the highest resonant frequency is around 35°.

The resonant frequencies from Figures 2.2a and 2.2b show that it is possible to trap a diamond micro-particle with a purely magnetic trap, as resonant frequencies larger than those for the magneto-gravitational trap can be engineered. However, due to experimental restrictions, it is not feasible to shape conical tips on magnets. As a compromise, we decided to shape the tips into square pyramids. Repeating the same modelling for square pyramid tips, we produced Figures 2.3a and 2.3b. These plots show similar trends to Figures 2.2a and 2.2b. There is once again an optimal angle of ascension that will maximise the resonant frequency of the diamond in the trap. This angle is the same for both axial and radial resonant frequencies, at 28.75°. This differs to the optimal angle from the conical tip case. This is likely due to the change in distribution of magnetic material from the change of number of sides.

Now, in the conical case, we assumed that the magnetic field was axially symmetric because the magnets were axially symmetric. However, square pyramid tipped magnets are no longer axially symmetric. One might expect to see a break in rotational symmetry of the magnetic field in the radial plane, which might lead to two different radial trapping frequencies. To check whether the magnetic field is axially symmetric, we examined the field in the central horizontal plane - that is, the radial plane equidistant from the points of the magnet tips. This is shown in Figure 2.4. As can be seen, the magnetic field is still completely axially symmetric in this plane, so that we are justified in considering

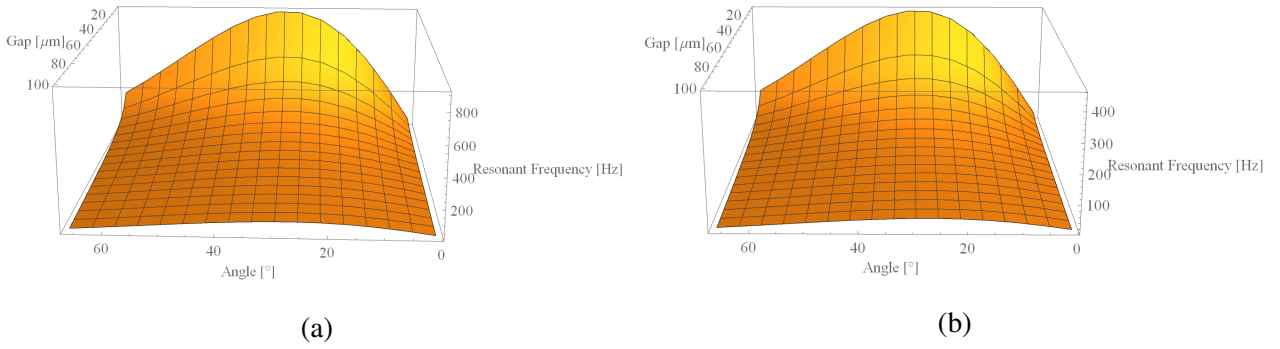(a)   (b)

Figure 2.3: Resonant frequency for a diamond micro-particle in the (a) radial and (b) axial modes, for a square pyramid tip magnetic trap, as a function of gap size and angle of tip ascension. The angle that gives the highest resonant frequency is 28.75° in both plots. This differs from the optimal angle found in Figure 2.2. This is because the material in the square pyramid tip with an angle of ascension of 28.75° will be equal to that of a conical tip with 35° angle of ascension.

the resonant frequencies for diamond of only 2 modes in this trap, as there are only 2 modes still.

With the tools we have made, we can optimise the diamond resonant frequency of our ideal square pyramid tip magnetic trap, as seen in Figure 2.5. Setting the angle of ascension to the optimal angle from Figures 2.3a and 2.3b, 28.75°, we find the relation between resonant frequency and gap size for both the axial and radial modes, shown in Figure 2.6. This shows that, like the angle of ascension, the resonant frequencies of both modes follow the same trend, with the axial frequency appearing to be approximately twice the radial frequency for any gap size. This allows the gap size to be chosen to suit our needs. For as strong a trap as possible, we will choose as small a gap size as possible, but which is still large enough to allow particles to be launched into the trap. We also cannot choose a gap size that is too small, as the repelling force from the magnets can be so large as to make creating the trap practically impossible. With these considerations in mind, we chose a gap size of 28 μm. This gives us an axial resonant frequency of 340 Hz, and a radial resonant frequency of 170 Hz.

To this point, we have ignored the effects of gravity for our trap. However, gravity could shift the centre of the trapping potential significantly. We therefore consider the shift of the potential due to gravity, which preserves the harmonicity of the trapping potential

$$U_{\text{tot}} = A(\tilde{x})^2 - C = U_{\text{mag}} + U_{\text{grav}} = \frac{1}{2}m\omega_0^2 x^2 - mgx, \tag{2.3}$$

where $\tilde{x}$ is of the form $\tilde{x} = x + G$, g is the acceleration due to gravity, taken as 9.8 ms^{-2}, and A, C, and G are constants. Choosing to align the trap such that the axial mode aligned exactly with the force due to gravity, such that we take $\omega_0 = 340$ Hz and solving this for G gives $g/\omega_0^2 = 2.1$ μm. Therefore
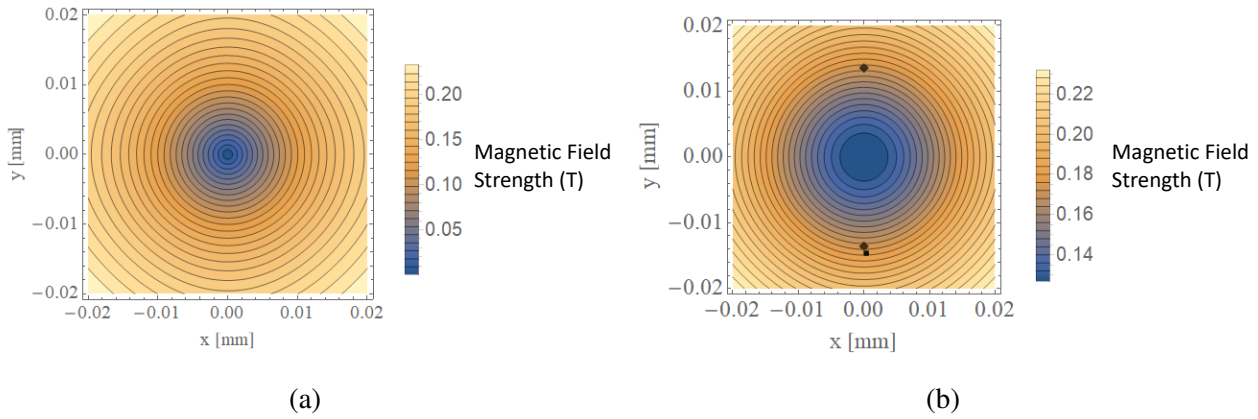
Figure 2.4: Magnetic field strength for square pyramid tip magnet trap, in the horizontal plane (a) halfway between the tip points, and (b) 10 μm up from the centre plane. This shows that the edges of the faces of the pyramid tip do not change the shape of the magnetic field, but that it is axially symmetric, such that there is only one horizontal mode - the radial mode. The blotches in (b) are modelling discrepancies.

the trapping potential is shifted down by 2.1 μm due to the force of gravity.

We have shown the conical tipped trap and the square pyramid tipped trap both produce resonant frequencies capable of trapping a diamond micro-particle. The modelling allowed for optimisation of the angle of ascension of the tip, and to find the resonant frequency for a chosen gap size. A square pyramid design was chosen, with an angle of ascension of 28.75° and a gap size of 28 μm, producing an axial resonant frequency of 340 Hz and a radial resonant frequency of 170 Hz. Furthermore, the shift in the trapping potential due to gravity was calculated, and found to be 2.1 μm.

2.3 Simulation of a Magnetically Trapped Diamond Micro-Particle in One Dimension

Having optimised the design of the magnetic trap, the kinetics of a diamond micro-particle will now be numerically simulated. This data will be analysed, compared with the theory, Brownian motion observed, and the effects of the trap considered.

Using the resonant frequency of diamond in the ideal square pyramid trap modelled previously, we can simulate the kinetics of a trapped diamond particle. However, we will only simulate the kinetics for one dimension. With the trap oriented such that the axial axis is vertical, the experimental detection system will measure the movement of the particle in the horizontal direction. As such, we
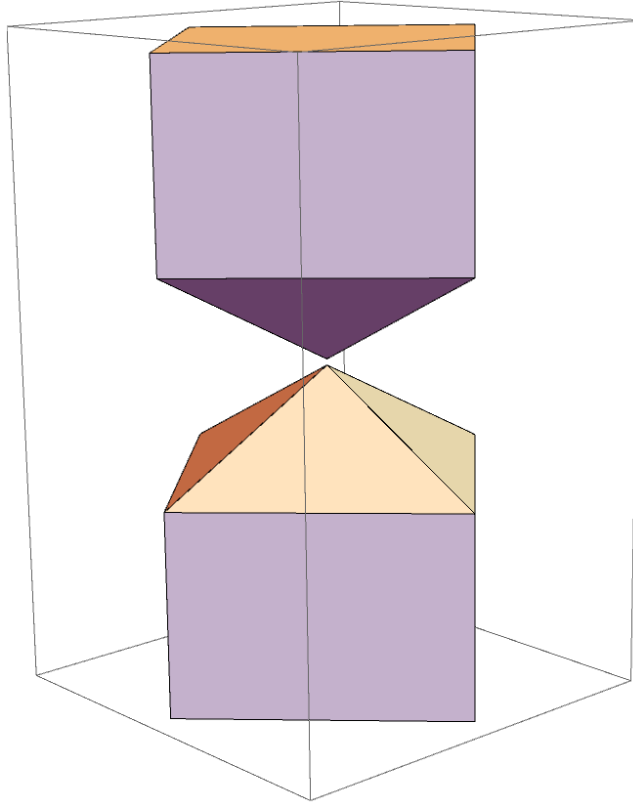
Figure 2.5: Model of the ends of the magnet tips. These magnets have the same pole facing each other, and are shaped to square pyramids at the tip. These magnets are 28 μm apart.

will simulate the kinetics of a diamond particle under the effects of the radial potential. This will not include the effects of gravity, which are assumed to not change the resonant frequency of the radial mode.

Firstly, we need to calculate the parameters we will be using in our simulation. We will use the radial frequency of 170 Hz found by the three dimensional modelling. We will need a temperature, so we will assume the gas in the (simulated) vacuum chamber is always at thermal equilibrium at room temperature, taking this to be $T = 298.15$ K. We must calculate the damping coefficient of the gas Γ_0, so will use the formula given in previous work [17],

$$\Gamma_0 = \frac{6\pi\eta r}{m} \frac{0.619}{0.619 + K_n}(1 + c_K), \tag{2.4}$$

where $K_n = l/r$ is the Knudsen number, where l is the mean free path of the gas molecules, r is the radius of the particle, and $c_K = (0.31K_n)/(0.785 + 1.152K_n + K_n^2)$ [17]. Thus we need to calculate the mean free path, so we will use the formula from kinetic theory
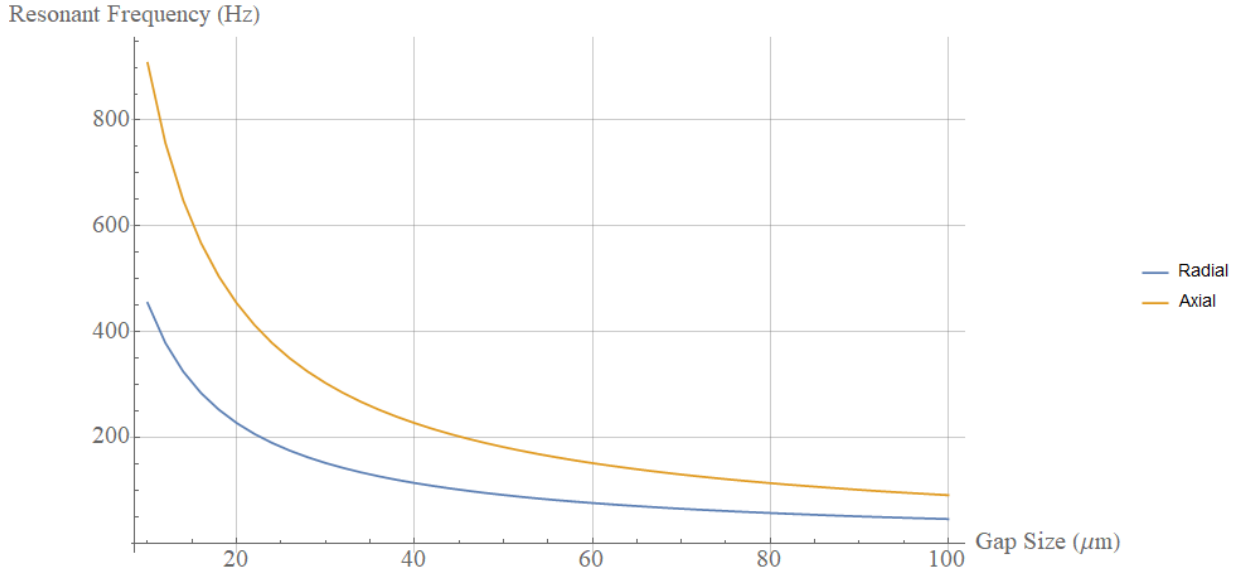
$$l = \frac{k_B T}{\sqrt{2}\pi d^2 p}, \tag{2.5}$$

Figure 2.6: Resonant frequency for a diamond micro-particle in a square pyramid tip magnetic trap, with angle of ascension of 28.75°, as a function of gap size. It is clear that no particular gap size is necessary to optimise a ratio of radial resonant frequency to axial resonant frequency, which appears approximately constant at 1:2.

which assumes the gas molecules behave like hard spheres of diameter d, like an ideal gas. For d, we will use the kinetic diameter of molecular nitrogen, 364 pm [26]. The pressure p is our independent variable to choose as we will. r is taken as 1 μm, as this is the average size of our individual diamond particles, and m is the mass of the trapped particle. This is calculated to be 1.3×10^{-14} kg, approximating the shape of the particle as spherical, and assuming the particle has the density of bulk diamond, 3150 kgm^{-3} [27]. T is the temperature taken as 298.15 K. The viscosity coefficient of air η is taken for the value at 25°C, which is 18×10^{-6} Pa s [28]. Γ_0 was calculated for various pressures covering our experimental pressure range, from 1.0×10^3 Torr (the measurement of atmospheric pressure by our thermocouple pressure gauge, though atmospheric pressure is truly 760 Torr) to 1.2×10^{-6} Torr.

With our parameters in hand, we used XMDS2, a numeric differential equation solver, to simulate the kinetics of the trapped particle in one dimension [29]. Specifically, the program was given the following Langevin equation:

$$\frac{\mathrm{d}^2 x}{\mathrm{d}t^2} = \frac{\sqrt{2m\Gamma_0 k_B T}}{m}\zeta_n - \Gamma_0 \frac{\mathrm{d}x}{\mathrm{d}t} - \omega_0^2 x, \tag{2.6}$$

where ζ_n is Wiener noise, such that the first term simulates the thermal noise which drives the Brownian motion, the second term is the damping due to the air, and the third term is the mass-normalised force on the particle due to the trapping potential. The simulations use the Runge-Kutta integration algorithm with fixed step size, which is correct to the fourth-order in the step size. The particle is given as initially stationary at the centre of the potential;

$$x(t = 0) = 0, \left.\frac{dx}{dt}\right|_{t=0} = 0. \tag{2.7}$$

The simulation solves for 2 blocks: the first block is to ensure the particle has time enough to thermalise from rest at the lowest pressures, solving for the first 500 seconds of motion, with step size of 5 μs; the second block serves as the measurement block, generating the output kinetic data by solving for the next 600 seconds of the particle's motion with the same step size. The kinetics data output by the second block is time and position data for 60 million equally spaced instances.

Once the data is simulated, it can be analysed in MATLAB and compared to the theory. The theory for the power spectral density of a Brownian particle in a harmonic trap is given in previous work [17],

$$S(\Omega) = \frac{2k_BT}{m} \frac{\Gamma_0}{(\omega_0^2 - \Omega^2)^2 + \Omega^2\Gamma_0^2}, \tag{2.8}$$

where Ω is angular frequency. We found the simulation power spectral densities (PSDs) to follow a similar trend to theory. A selection of the simulation PSDs and theory for chosen pressures is presented in Figure 2.7. This plot shows that the simulation has the same basic shape as the theory; a flat starting baseline, some sort of peak around the resonant frequency, and then the roll-off in power for frequencies greater than those forming the resonant peak. These features are properties of Brownian motion. The simulation also follows the trend of the power of the starting baseline decreasing with decreasing pressure. Furthermore, there is agreement in the trend of the shape of the resonant peaks at 170 Hz with changing pressure; the change in pressure results in a narrower, taller peak as the pressure decreases in both the theory and the simulation.

However, it is also clear that there are differences between the theory and the simulation PSDs. It seems that, as the pressure decreases, the baseline power of the theory drops further below the simulated PSD's baseline power. This is possibly due to the limitations on the calculation of the PSD from the simulated data. This limitation is a trade-off that must be made between noise in power and resolution in frequency, such that as noise is decreased, the frequency resolution is increased, and vice versa. The noise in power occurs because of the simulated thermal noise, and is reduced by dividing the kinetic data into equal subsets. These subsets produce a PSD each, and the final PSD is obtained

by averaging them all. Therefore, we reduce the noise in power by dividing into more subsets, but this sacrifices frequency resolution. The chosen balance was for 12 data subsets, giving the noise seen in Figure 2.7, and a frequency resolution of 20 mHz.

The other difference between the simulation PSDs and the theory seen in Figure 2.7 is that of the roll-off. The theory shows a monomial-like relation after the resonant peak between frequency and power, which has the same slope regardless of the pressure. However, while the the roll-off from the simulation PSDs is largely monomial-like, the slope changes when at the lowest pressure, such that it has a gentler slope. Note that the plateau after 4×10^4 Hz is an artefact caused in producing the PSD. This may be the lower power limit of this PSD. As such, the roll-off of the lowest pressure simulation PSD heads directly to this limit at 4×10^4 Hz, and so the explanation for the change in slope may be that the PSD is limited by the lower power limit.
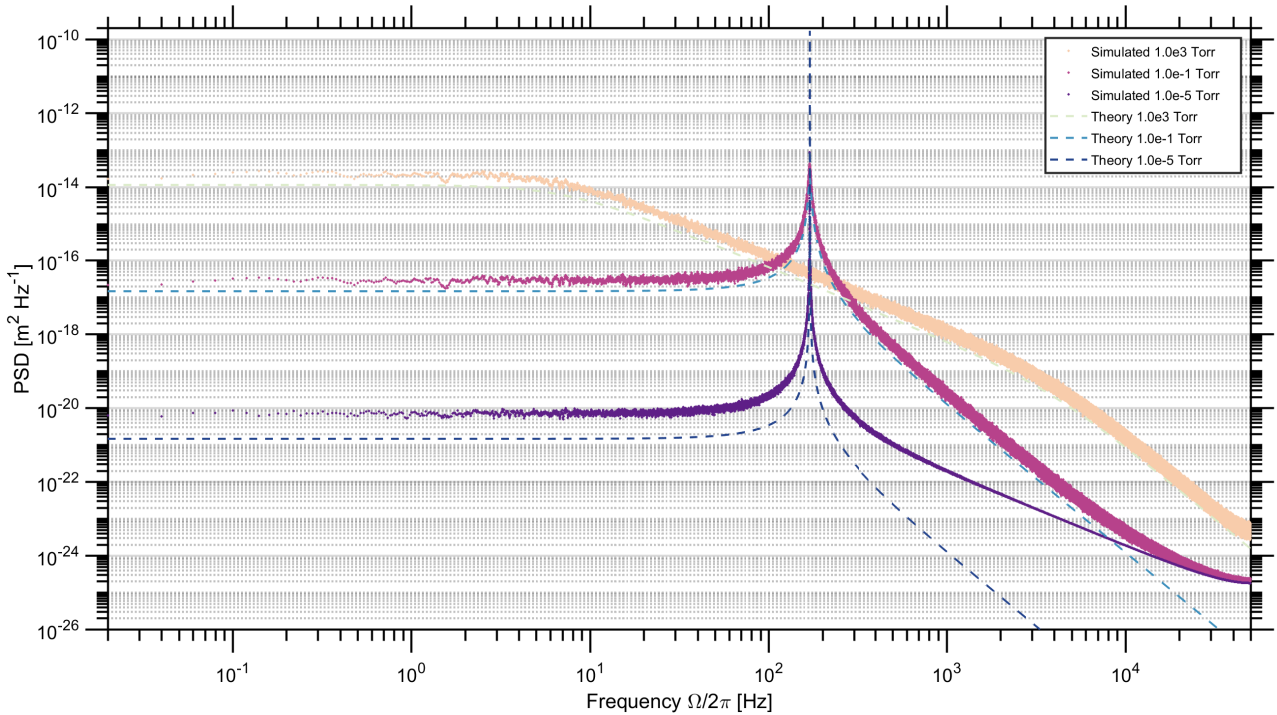

Figure 2.7: Power Spectrum Densities (PSDs) of the simulated data for the selected pressures, and the theory at corresponding pressures. The general shape of the simulation PSDs match the theory well, with differences only in the power values, and the shape of the roll-off after the resonant peak. The difference in power values is likely an effect of noise, while the roll-off difference is possibly due to the lower power limit of our evaluation of the simulation MSDs, seen above 40 kHz.

The simulation data was also used to produce Mean Square Displacements (MSDs), which were

compared to the theory for the MSD of a Brownian particle in a harmonic trap, given by the formula

$$\langle [\Delta x_{\text{tra}}(t)]^2 \rangle = \frac{2k_B T}{m\omega_0^2} \left(1 - \exp\left(-\frac{t}{2\tau_p} \right) \right) \left(\cos(\omega_1 t) + \frac{\sin(\omega_1 t)}{2\omega_1 \tau_p} \right), \tag{2.9}$$

where $\omega_1 = \sqrt{\omega_0^2 - (1/2\tau_p)^2}$, where $\tau_p = 1/\Gamma_0$ is the momentum relaxation time of the air. The MSDs at select pressures are shown in Figure 2.8. From this we see that the simulation MSDs fit the theory exactly. The highest pressure MSDs (at 1.0×10^3 Torr) show the diffusive regime, and at short time scales agree with Einstein's formula for the MSD, given by $\langle [\Delta x_{\text{dif}}(t)]^2 \rangle = 2Dt$, where $D = (k_B T/\Gamma_0 m)$ is the diffusion coefficient. At long time scales, these MSDs tend to a constant due to the trapping potential. For the lower pressure MSDs, we observe the ballistic regime. At short time scales, the simulation MSDs follow the same t^2 slope indicative of the ballistic regime. At long time scales, the simulation MSDs converge to a constant value, again because of the trapping potential. At intermediate time scales, the MSDs oscillate with decaying amplitude, with the oscillation frequency depending on the resonant frequency. At the lowest pressure, we see the peak to peak amplitude oscillate, and very little decay is seen at all, as the pressure is so low that only the short and intermediate time scales are produced for this MSD.

Thus we have simulated the motion of a diamond micro-particle in our ideal, harmonic trap. It has been seen that the simulated PSDs match the theory fairly well, with some differences in power level and the behaviour at frequencies over those for the resonant peak. The simulated MSDs match the theory exactly, and show interesting behaviour at the lower end of our pressure range.

In this chapter, we have used modelling to prove that an appropriately engineered, purely magnetic trap may trap diamagnetic micro-particles. Further modelling showed how this trap could be designed, by optimising the shape of the magnets used, resulting in a more practical design which takes experimental considerations into account. The modelling allowed this ideal trap to be characterised, by finding the resonant frequencies for diamond micro-particles in both harmonic fundamental modes, the values of which were 170 Hz and 340 Hz. These frequencies are larger than those of the magneto-gravitational trap, which was successful at trapping diamond nano-particles. This indicates that our trap should be able to trap diamond micro-particles. Simulations of the kinetics of a particle using the trap characteristics for a pressure range spanning 8 magnitudes, down to 1.0×10^{-5} Torr, agreed well with the theory. As such, we have found XMDS2 to be a reliable tool in simulating the Brownian motion, even at extremely low pressures, as the simulations agree with the theory. If the experimental results agree with the simulations, the 3 dimensional modelling will be validated, proving the 3 dimensional modelling an accurate tool for further magnetic trap designs.
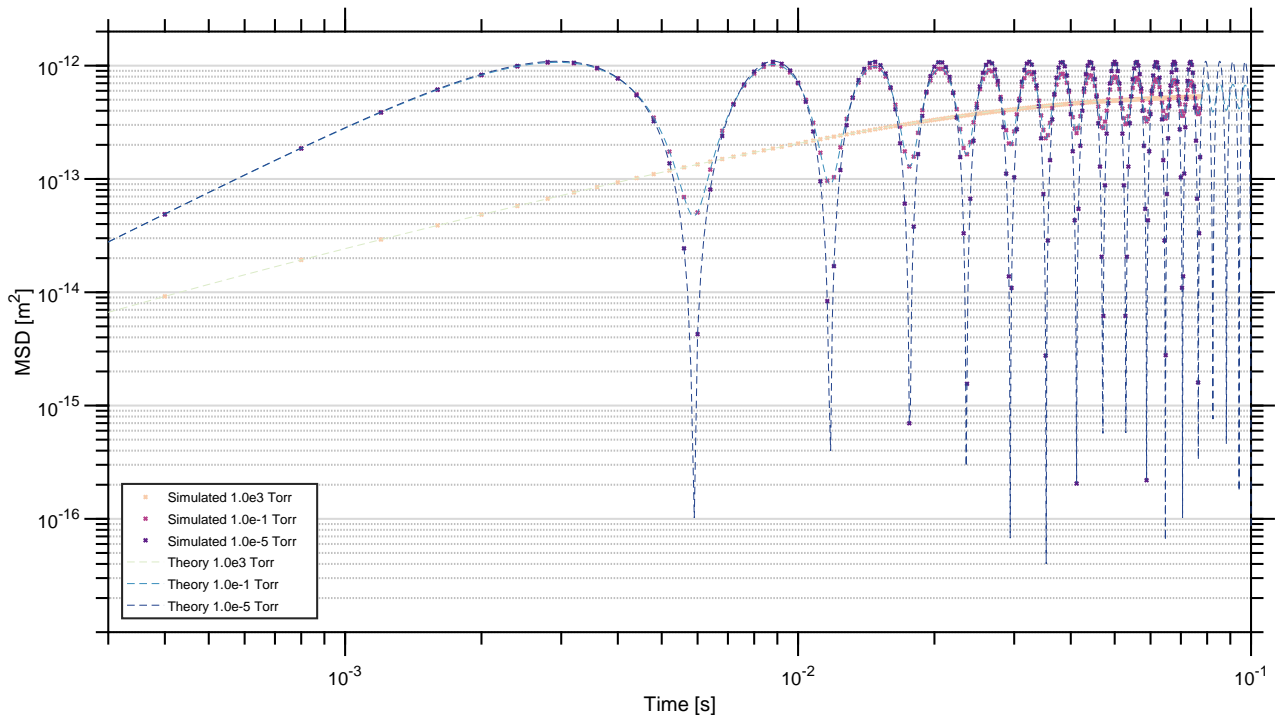
Figure 2.8: Mean Square Displacements (MSDs) of the simulated data for the selected pressures, and the theory at corresponding pressures. The highest pressure data shows the diffusive regime, while the lower pressures show the ballistic regime. The simulation MSDs match the theory extremely well. The MSDs converge to a constant value at long time scales due to the trap. At short time scales, the highest pressure MSDs have a slope proportional to t, while the lower pressures are proportional to t^2.

3

Experimental

In this chapter we will discuss the experimental setup of the project, starting with the practicalities of building the magnetic trap, including shaping and positioning the magnets. Following this we will briefly mention how the trap is positioned in the vacuum chamber, and the main specifications of interest of the vacuum system. A detailed discussion of the optical system then follows, as there are many components and practicalities to mention. This is an important system as the optical system is instrumental for measuring the motion of the trapped particle. Following this discussion is a section on the material choice of particles and their properties, as well as the description of the particle loading procedure. Finally, the active feedback cooling system is described.

3.1 Building the Magnetic Trap

The magnetic trap is formed by two faceted magnets, positioned with like poles facing each other around 20 μm apart. The two magnets are glued to an alumina strip, with a hole cut through it for optical access to the trap region. This hole also allows particle loading. This assemblage is coated in

1 μm thick layer of gold by evaporation deposition, to alleviate the build up of electrostatic charge.

Each magnet was polished to the shape of a square prism, with a tip in the shape of a four sided pyramid. This design was discussed in Chapter 2. The apex of this pyramid was aimed to be of the order of a micron across. This is around the sharpness limit of the tip, as the magnets are rare earth, Neodymium Iron Boron (NdFeB), and therefore made from a sintered powder. Consequently, the material has a granular structure, and is quite hard. The magnets were polished to the desired shape using a gemstone faceting machine, with diamond grit plates run at a low revolution rate and oil cooling lubrication. Previously we had tried laser machining and standard machining techniques. The gemstone faceting machine allows for precision shaping, while the lubrication and low revolution rate kept the surface of the magnet below the critical temperature of 40°, over which the material demagnetises. The process of shaping the magnets was quite a challenge, and was a key part of the project, as the shape of the magnets and the field strengths at the magnets' surfaces are instrumental to the shape of the magnetic field, and so the magnetic trap.

These NdFeB magnets are very powerful, with a 2 T magnetic field produced from the tips, as can be seen in Chapter 2. As such, when in the trapping configuration described (producing an anti-Helmholtz magnetic field), the repelling magnetic forces are substantial, making positioning and holding the magnets in place a non-trivial affair. The alignment of the tips was essential in producing the modelled trap, and proved challenging. In the end, a micro stage from Thorlabs was purchased and a custom magnet holding rig was used. Thus, after the first magnet was glued to the alumina strip, the second magnet could be positioned with 50 nm precision. The trap was then positioned in a small vacuum chamber with optical ports, as we wish to change the pressure and nature of the gas surrounding a trapped particle.

3.2   Holding the Trap in the Vacuum Chamber

The trap was fitted into an aluminium holder at an optical port. The aluminium holder had an optical access hole, and an adjoining hole for loading the particle. The windows for this chamber are usually around 4 mm thick, but as this is the working distance of our microscope objective, the window which the trap was up against had to be redesigned. The design implemented was to fit a smaller window frame into the existing frame, producing a smaller area for the window. This lowered the force on the window, allowing for a thinner window. This replacement window was made from a 330 μm thick piece of sapphire crystal.

3.3 The Vacuum System

The vacuum system used in this project was small, with optical ports. Two pumps were used: a dry mechanical pump for atmospheric to low vacuum pressures, and a 90 L/s turbomolecular pump for higher vacuum pressures. Two vacuum gauges were used to monitor the pressure range covered. A leak valve was used in concert with these gauges to control the pressure over the range of 1×10^3 Torr to 1×10^{-5} Torr.

3.4 The Optical System

To observe the trapped particles, an optical system is used, as presented in Figure 3.1.
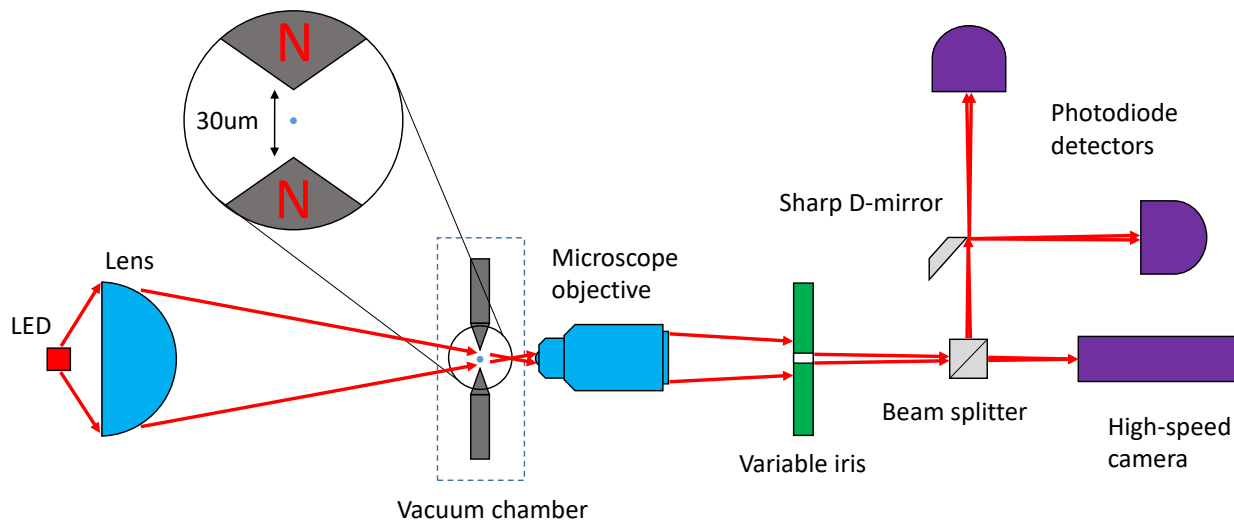

Figure 3.1: A schematic of the apparatus. The light from the red light emitting diode (LED) is collected and directed by the lens onto the trapping region in the vacuum chamber. This light is then collected by a long working distance microscope objective, which magnifies the trapping region. A variable iris is used to narrow the beam to the area the trapped particle can occupy. A beam splitter sends half of the beam to a high-speed camera, and the other half to a detection system. This detection systems consists of a sharp-edged D-mirror, upon which the image of the particle is formed, and which cuts the image in half, reflecting one half to one photodiode detector, and the other half to another photodiode detector.

The apparatus was covered in a dark sheet to reduce noise in the optical signal, as the spectrum of

the room lighting contains a non-trivial contribution at the wavelength of the optical signal. Unlike the research discussed in Chapter 1, our light source is an LED, not a laser. This reduces noise by eliminating the speckle pattern of a laser, and does not heat the motion of the particle.

To collect the light from the trapping region so that information of the particle's position can be measured, a microscope objective is used. However, as the particle is in the vacuum chamber, and the microscope objective is not, placing a sapphire window between the two, an objective with a long working distance is required. The objective we used is a metallurgical objective, with a working distance of 4 mm. This objective produces an image of the trapped particle on the sharp edged D-mirror, as seen in Figure 3.1.

A beam splitter then directs half of the signal to a high-speed camera, and the other half toward the sharp edge of a D-mirror and a position measurement system. The camera is used to confirm the presence of a trapped particle, as well as the apparent size and shape of said particle. The camera must be high-speed because the resonant frequency of the trapped particles is of the order of hundreds of Hertz, so that a conventional camera cannot track the position of the particle accurately, due to aliasing. It should be noted that the particle on these images appears as a dark shape, rather than light, because this optical system tracks the movement of the particle's shadow. This is seen in Figure 3.2 important in considering the measurement of the particle's position. The image plane formed by the microscope objective falls upon the sharp edge of the D-mirror. This D-mirror cuts the image in half, allowing half to continue on to one photodiode detector, and reflecting the other half to the other photodiode detector. This piece of equipment is instrumental in detecting the particle's movement. Furthermore, the D-mirror must lie in the image plane created by the objective to form a clear image to bisect, which reduces the uncertainty of determining the transition of the particle over the bisecting line. Thus, the clearer the image on the D-mirror, the more sensitive our detection system is to measuring a signal related to the particle's position. As seen in Figure 3.3, the half of the image in which the shadow of the particle is undergoes a decrease in signal intensity. This allows us to track the position of the particle over some central line, determined by the alignment of the image signal on the sharp edge of the D-mirror.

The two halves of the image signal are collected by two photodiode detectors, converting the signal of light intensity into a voltage signal. These signals are sent to a bandpass filter and amplifier, where one is subtracted from the other, resulting in a position-related intensity signal in volts. This signal is digitised by a 14-bit Cleverscope oscilloscope, giving a dynamic range of 72 dB. The digital signal is then analysed on a computer. Next, the signal is analysed to produce the measure of the resonance
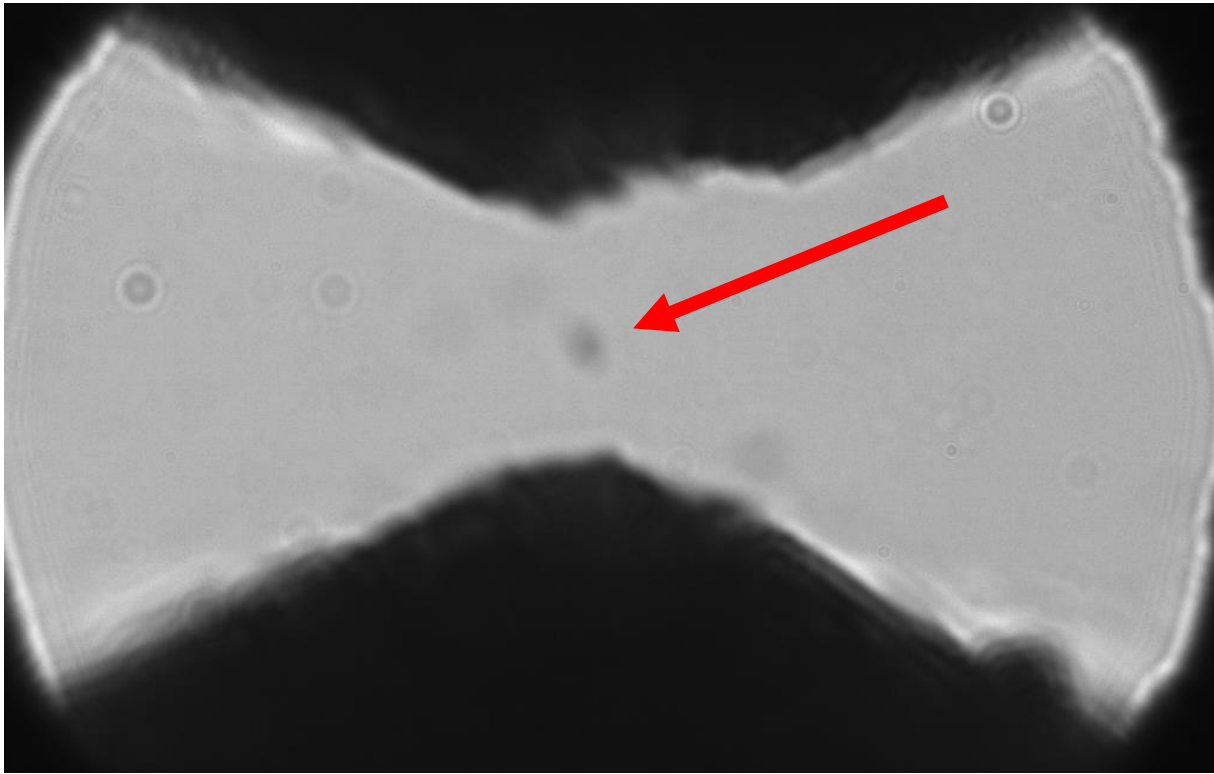
Figure 3.2: Photo from the high speed camera, of the trapping region. The arrow points to the trapped diamond particle. The tips of the magnets can be seen above and below, seen to be blunted rather than sharp as in the ideal trap design. Note that other blurs are particles stuck to the vacuum chamber window, or the magnets.

frequency of the trapping system, and the Brownian motion of the particle. However, the Brownian motion signal is much smaller than the resonance signal, such that the Brownian motion will appear as noise relative to the resonance signal. As such, to accurately measure the Brownian signal and nothing else, other sources of noise need to be minimised. One such noise source is room vibrations, which could shake both the vacuum chamber and the optical system to varying degrees, producing a significant false aspect to the position signal. To avoid this, the system is isolated from this noise somewhat by mounting the optical system and vacuum chamber on a floating optical table.

The main measurement device is the 14-bit Cleverscope oscilloscope. As mentioned above, this 14-bit capability gives a maximum dynamic range of 72 dB between the highest signal measured and the lowest signal measured (when the highest signal is almost overloading the oscilloscope). In reality, the noise-floor of the signal will reduce the practical dynamic range to something more like 50 dB. This will limit the feedback cooling signal, limiting the amount of cooling achievable. Additionally, as the mechanical quality factor of the system is expected to reach the thousands, and the resonant
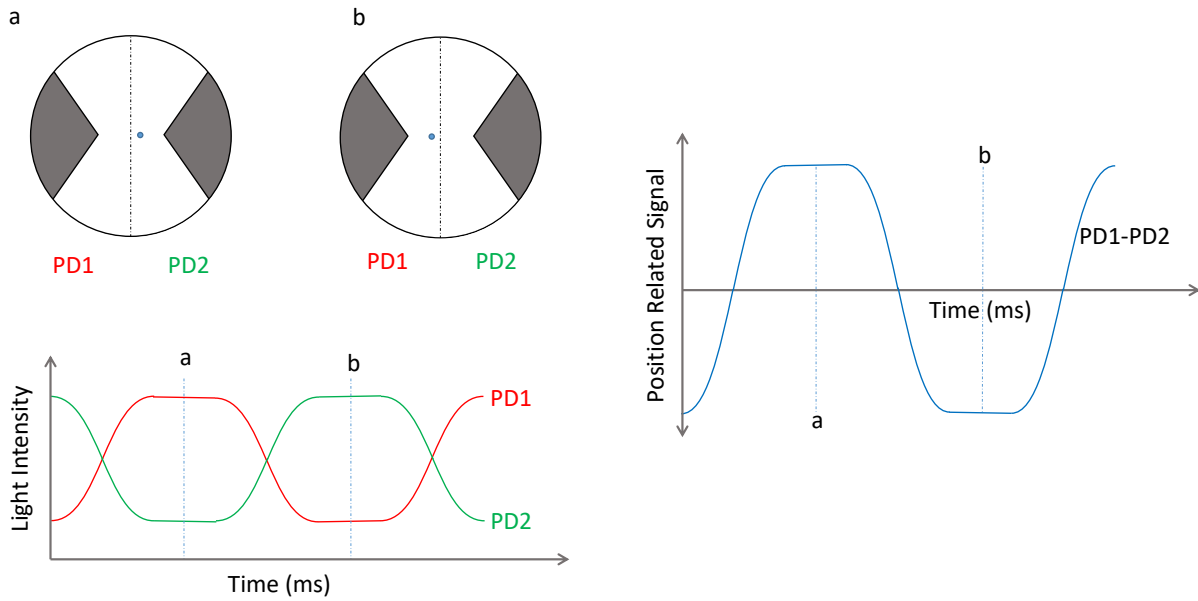
Figure 3.3: A demonstration of the detection system. The top left images show scenarios **a** and **b**, where the particle is fully on one side of the line bisecting the image. The bottom left image shows the approximate shape of the signal for each photodiode detector (PD1 and PD2) as the particle moves back and forth across the bisecting line. When the particle is fully on one side, as in scenario a or b, the signal becomes truncated, as no additional information of the position of the particle is measured.

frequency is of the order of 300 Hz, frequency resolution of milliHertz is required to measure the response of our system. The Cleverscope has a very steady, temperature controlled timebase, and high sampling rate. To achieve fine frequency resolution from our digitised signal, we require a high sampling rate, and many samples. Therefore, it becomes important for these samples to be evenly spaced in time, and the Cleverscope's steady timebase regulates that. Thus, the Cleverscope isolated oscilloscope helps to reduce uncertainty, and to quantify the uncertainty that remains.

It should also be noted that the intensity signal that we measure is not directly proportional to the position of the particle. The position of the centre of a spherical particle as it moves over a line will not be proportional to the area of the cross-section over that line. Instead, the relationship is non-linear.

3.5   The Particles

As discussed in Chapter 1, a magnetic trap requires a diamagnetic material. As mentioned earlier in this chapter, our trap consists of two sharp magnets producing a magnetic field in an anti-Helmholtz

configuration, and requiring a diamagnetic particle. The more strongly diamagnetic the particle material is, the stronger the trapping forces. As such, we first trapped pyrolytic graphite. This strongly negative magnetic susceptibility resulted in a strong trapping potential. However, this magnetic susceptibility value is in only one plane, with values in the other axes weaker by an order of magnitude. This anisotropy, together with the irregular shape of the particles, resulted in tumbling, widely varying motion, so that while the particles were strongly trapped, the motion, and by extension the resonant frequency of the trap, was difficult to measure. This resulted in an inability to characterise the magnetic trap using a pyrolytic graphite micro-particle. However, a more suitable material was chosen, which was used to produce all the experimental data in Chapter 4; monocrystalline diamond particles, from 1-2.5 μm in size. These diamond particles were purchased from Microdiamant, and were made by detonation processes. To prevent electrostatics from influencing the experiment, the particles were coated with thin conductive films by mixing in a consumer anti-static solution, then baking and breaking up the dried agglomeration.

The particles were loaded into the trap on a stream of gas, directed at the trap. Once a particle was trapped, the vacuum chamber was closed and sealed, and pumped down. This solution is likely to work uniquely for our trap, as our purely magnetic trap is more robust than optical traps or previous magnetic hybrid traps.

3.6   Cooling

The final section of this chapter is concerning the cooling of motion of the trapped particle. In Chapter 1 feedback cooling was discussed in both an optical trapping system, and the magnetogravitational system. While these two systems cool by different methods practically, both cool by altering the trapping potential slightly, shifting the centre of the trap away from the position of the particle. The magnitude of this shift is dependent on the measured velocity of the particle. We perform the same type of cooling in our experiment (the alternative is to strengthen and weaken the trapping potential depending on the particle's position). We used a feedback signal to drive a current through a pair of large coils outside of the vacuum chamber to manipulate the magnetic field. The measured position signal is differentiated and this is sent to a power amplifier, which performs the gain function for the signal. This drives an alternating current through a pair of Helmholtz coils, positioned either side of the trap, on the same axis as the magnets. This signal then shifts the centre of the trap dependent on the velocity of the particle.

4

Results

In this chapter, the experimental measurements of the kinetics of the trapped diamond micro-particle of the project will be presented and discussed in the following order: the data collection process will be outlined, followed by the presentation of the power spectral densities (PSDs) of non-cooled kinetics, and a detailed analysis and comparison of this data with regard to theory. Following this, the PSDs of the cooled kinetics will be presented and discussed, including an estimation of the centre of mass thermal temperature of the trapped particle and the limiting lowest temperature achieved. The mean square displacements (MSDs), both experimental and theory, will be presented and briefly discussed. We end with a statistical analysis of the lowest non-cooled experimental kinetics and a discussion of the observed behaviour within the confines of statistical mechanics.

4.1   The Data Collection

To gather the data of the particle's position as a function of time along the weak trapping axis, the particle was initially magnetically trapped at atmospheric pressure. Then the chamber was sealed, and

the pressure lowered until each target pressure was reached, at which point the pressure was stabilised and measurements taken. When the pressure was low enough so that when the magnetic feedback cooling system was turned on, the motion of the particle was damped noticeably along the cooled direction, as indicated by the measurement signal, data was also recorded with the cooling on. When these conditions were met, the cooling was left on as the pressure was lowered further, to ensure that the particle remained in the trap. When a suitable lower pressure was reached, the cooling was turned off and the particle was allowed 10 minutes to reach thermal equilibrium with its environment before any measurements were taken. These measurements are denoted "thermal kinetics". Data was recorded for at least a 10 minute duration during each measurement, with a sampling frequency of 100 kHz, producing over 60 million samples per measurement run.

The only exception to the described process was in reaching 1.0×10^{-3} Torr. The roughing pump alone could not lower the pressure any further than 1.9×10^{-2} Torr, so the turbo pump had to be turned on to lower the pressure further. The cooling was also turned on to ensure the particle remained trapped. However, pressure readings cannot be taken with the thermocouple pressure gauge when the turbo pump is operating. This is due to the positioning of the thermocouple gauge, such that it is cut off from the part of the chamber containing the trap when the turbo pump is operating. Furthermore, the cold cathode gauge cannot be switched on until the pressure is approximately 1×10^{-3} Torr. With no way to determine this pressure, the turbo and cooling were run for 10 minutes before the cold cathode gauge was turned on. At this point the reading on the gauge was two orders of magnitude lower than the target pressure, and so the pressure had to be raised substantially, after which the cooling could be turned off. After this, the procedure described earlier was followed to attain the other target pressures.

Finally, a dataset was also recorded with no particle in the trap, at very low pressure (2.3×10^{-6} Torr) to account for the noise in the detection system.

4.2   Non-Cooled PSDs

Each dataset was divided into 12 equal subsets, and a PSD produced for each subset. These 12 PSDs were then averaged to produce the final spectrum for that measured data, with 20 mHz resolution. Producing the PSD of a larger dataset results in lower frequency resolution. However, such a PSD will have a lot of random noise. This random noise is reduced by the averaging process, and so a balance was found between the frequency resolution and the amount of manageable random noise.

We will briefly justify the choice of the frequency range for the PSDs, an example of which is 4.1.

At the low end, the bandpass filter attenuates the signal for frequencies less than 10 Hz. This is also the case at the high end for above 10 kHz. This is also the region where we reach the noise floor of the detection system (that is, the lowest levels that the system can detect). This region is dominated by noise, and no features are discernible, much like the region above 2 kHz.

The PSD for the data when no particle was in the trap gives an indication of the noise in the measurement system. With reference to Figure 4.1, the peaks at 50, 100, and 120 Hz are from line noise, the fluorescent room lights, and the computer monitor refresh rate, respectively. Harmonics of these noise peaks can also be seen through the spectrum, particularly when the line noise and room light harmonics align. Mechanical vibrations such as from the turbo can be seen at 1500 Hz, and other sources of noise such as room noise not dampened enough by the optical table are likely present in this spectrum. Interesting peaks in the noise PSD to make a note of are the peaks which are not narrow, primarily that at 125 Hz, and, to a lesser extent, at 168 Hz. The sources of noise for these peaks are unknown, but it seems that this noise drives the motion of the particle in the trap, as most of the other spectra at these points have higher amplitudes than the noise spectrum. The noise at these frequencies is probably a mechanical vibration. This would either move the trapping magnets, driving the motion of the trapped particle, or move parts of the detection system, such as the D-mirror. The latter scenario would only make it appear that the motion of the particle is being driven because of a shift in the line which bisects the image of the particle, and so defines the signal measured. It should also be noted that there is additional noise generated from the turbo pump not captured in the noise spectrum. This noise is from the turbo pump when running in standby mode (at 70% of full speed), which was only for the 1.0×10^{-3} Torr and 1.0×10^{-5} Torr measurements, as seen in Figure 4.4. The turbo pump was running at full speed when the noise dataset was recorded, so the peak is at 1500 Hz, as seen in Figure 4.6 rather than 1050 Hz.
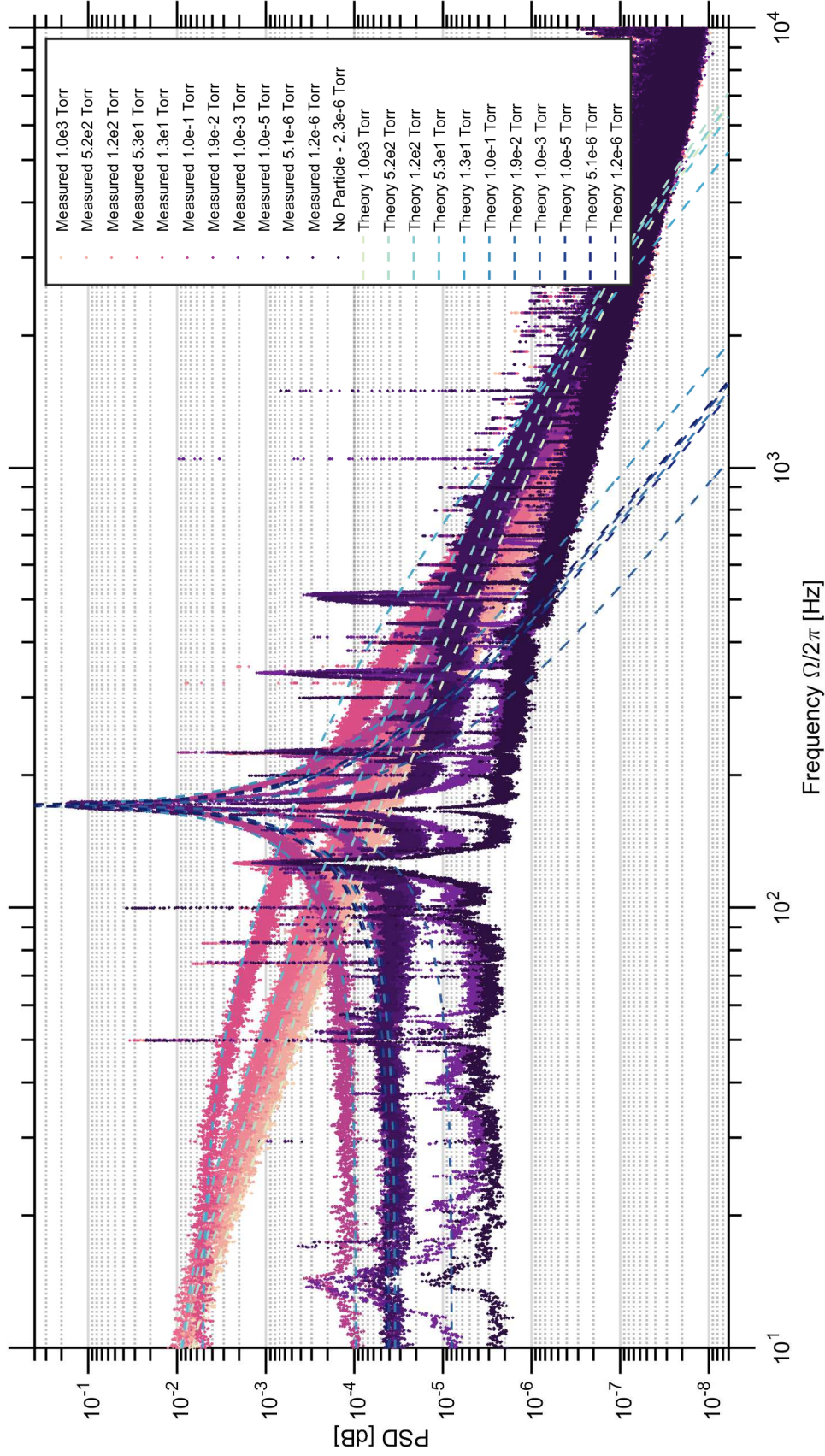
Figure 4.1: Power spectral density of all measured data (dots), expected spectra (dotted lines) and the spectra taken when no particle was in the trap, which represents the noise in the signal. From this plot we can see 3 regimes: the spectra which fit the theory well; the spectra which do not fit the theory after the resonant peak near 170 Hz, but which agrees elsewhere; and the spectra which do not follow the trend of decreasing general amplitude with decrease in pressure. This plot shows the broad scope of the data [30].

Each theoretical prediction for a one dimensional harmonic trap was scaled to match the amplitude of the corresponding spectrum at low frequencies. The unscaled PSDs from simulated data are shown in Figure 4.2. From Figures 4.1 and 4.2 we can identify the three observed regimes. The highest pressure regime is that which shows fair agreement with the simulation, seen in Figure 4.3. The next regime is defined by its fair agreement with the simulation until after the resonant peak at 170 Hz. Other than that, the observed peaks are shorter and wider than the simulated peaks. Comparing Figures 4.1 and 4.2, we also see that while we expect the amplitude of the baseline of the spectra to keep decreasing with decreasing pressure, it instead increases for the 3 lowest pressures. Therefore, we split the spectra into 3 regimes: the highest pressures, seen in Figure 4.3, which match the simulations well; the middling pressures, seen in Figure 4.4, which agree with simulations in the trend of decreasing baseline amplitude and show a resonant peak; and the lowest pressures, seen in Figure 4.6, which only partly agree with the shape predicted and in which the amplitude of the baseline rises with decreasing pressure.
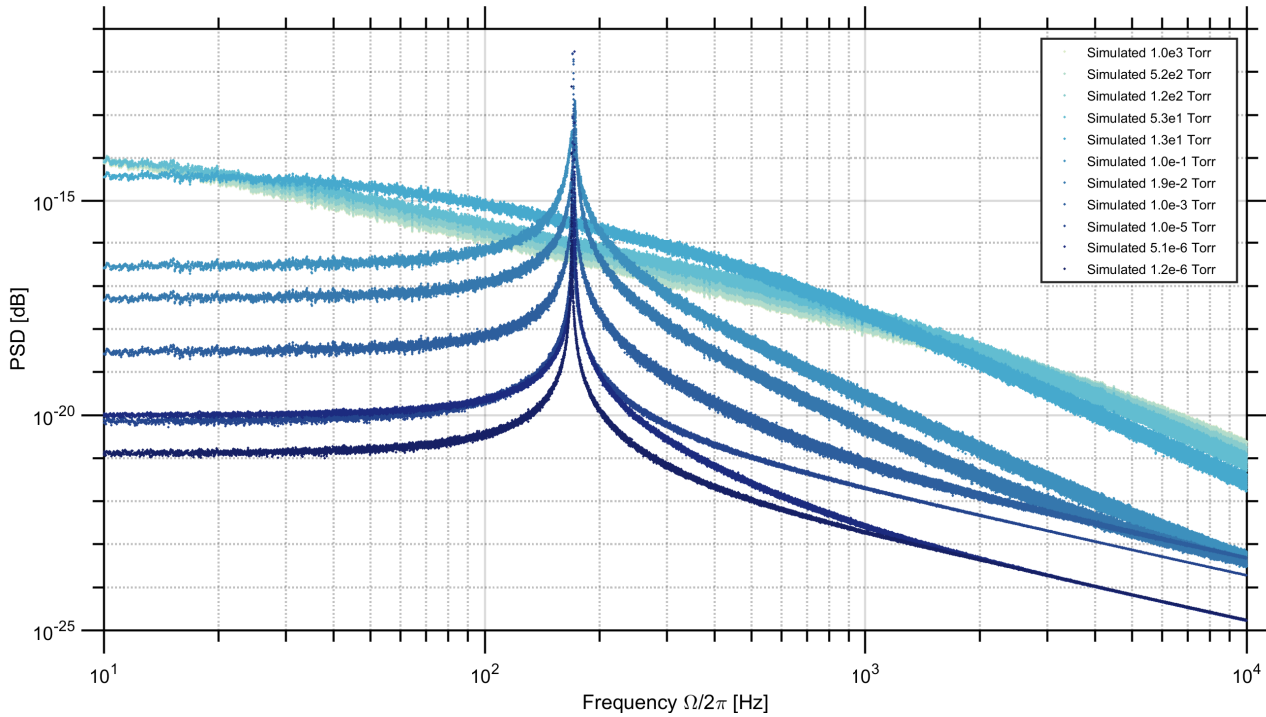

Figure 4.2: Power spectral density of all non-cooled simulated data (unscaled). Compare with Figure 4.1 to see the deviation from the expected results in terms of baseline amplitude.

4.2.1   The High Pressures

The high pressure regime, seen in Figure 4.3, agrees very well with the theory in all features, with difference at high frequency because of the dynamic range of the detection system. The data slope changes around 400 Hz, falling faster than the simulation at those frequencies. It isn't until the simulation reaches $1-2$ kHz that it changes slope, by which time the simulation has reached the limit of the detection system. At the lowest measured pressure in this regime - 1.0×10^1 Torr - the trend of the data changes, so that both the recorded and the simulated spectrum roll off from the baseline value, with slopes matching extremely well before the recorded spectrum reaches the detection limit. The only discrepancy at this pressure is the frequency at which the roll off starts. This is likely due to some slight variation in the trapping frequency in the physical trap, which may be caused by wandering over time, variation in temperature, or slight shifts in the trapping magnets. This variation is difficult to detect in this regime, as there is no well defined resonance peak.
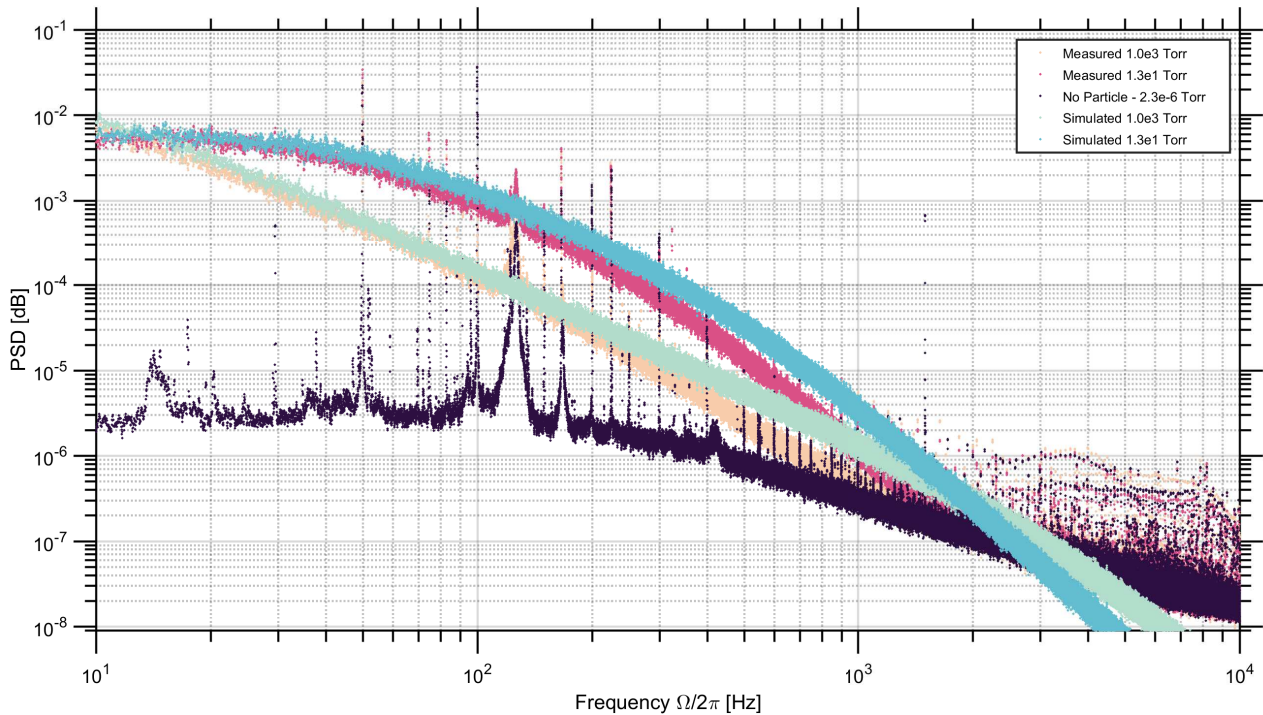

Figure 4.3: Power spectral density of selected high pressure spectra, with measured and simulated data.

4.2.2 The Middling Pressures

In the middle pressure regime, seen in Figures 4.4 and 4.5 we can see the resonant frequency forming a peak in both recorded and simulated spectra. The variation of the resonance frequency suggested previously can be seen in this regime, with the peak centred around 171 Hz. The simulations' resonant peak is taller and has a wider base than the measured peak at each pressure in this regime, with the height and base-width increasing as the pressure decreases. This indicates that the recorded spectra have larger damping coefficients than the simulations. Since the simulations use values of Γ_0 calculated from the measured pressures, this would indicate that the measured pressure is not the pressure the trapped particle experiences. By finding the relation between the height of the baseline and the height of the resonant peak from the theoretical formula of the spectrum,

$$S(\Omega) = \frac{2k_B T_0}{m} \frac{\Gamma_0}{(\omega_0^2 - \Omega^2)^2 + \Omega^2\Gamma_0^2},$$

(4.1)

we find

$$\frac{S(\omega_0)}{S(0)} = \frac{\omega_0^2}{\Gamma_0^2}.$$

(4.2)

While there is a large relative uncertainty associated with the pressure measurement (around 20%), this does not account for the damping coefficients necessary to match the recorded peak. However, it is likely that the pressure measurement does not represent the pressure in the trapping region, as this is quite a confined space, and it is known that confined spaces have higher pressures. This may be enough to account for the difference between the recorded and simulated shape of the peak.

Note that peaks can also be seen around 225 Hz, seen in Figure 4.5, which also vary in frequency for different measurements. These peaks are interpreted to be the resonant frequency in the direction of the beamline - the parallel dimension. In the ideal case, the magnets are shaped to a perfect point, and are symmetric under a rotation of $\pi/2$ around the axial axis. However, the shaping process not perfect, and the final magnets have tips that are more like slightly blunted wedges than perfect sharp pyramids. Thus, instead of one radial resonant frequency, there are two. These peaks around 225 Hz are thought to be this parallel frequency. The amplitude of these peaks is likely not small because of low occupancy of this mode, but because the detection system is not designed to detect motion in this dimension well. There is another noise peak inside this supposed resonant peak, so it is possible that this motion is being driven by the noise, similarly to the previously discussed primary resonant peak.

Other new peaks have emerged in this regime, namely harmonics of the resonant peaks. There are noticeable peaks around 510 Hz (3 times the primary resonant frequency), and even small peaks around 440 Hz (roughly twice the parallel resonant frequency). In this regime, the simulation spectra
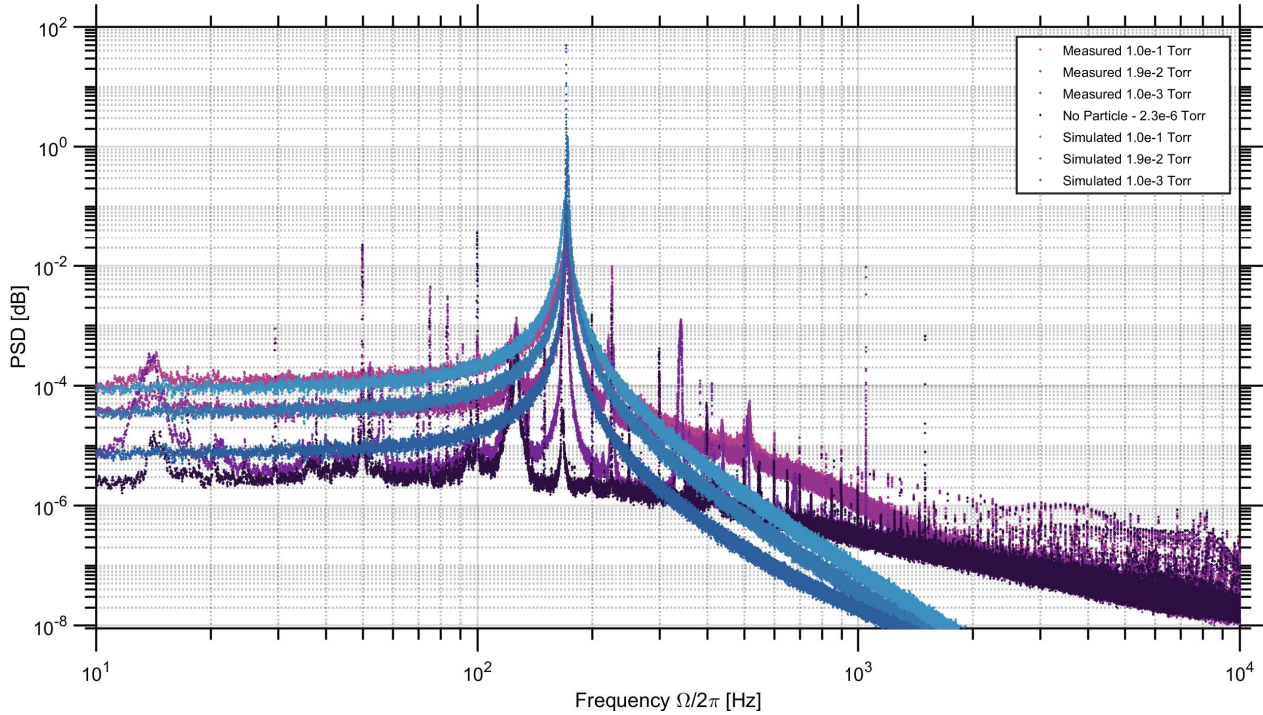
Figure 4.4: Power spectral density of middling pressure spectra, with measured and simulated data.

after the peak drops away with a large gradient, while the recorded spectra has a small gradient until around 900Hz. This is similar to the higher pressure regime, and could be detection of the axial frequency. The spectrum at 1.0×10^{-3} Torr is a special case, which will be discussed presently.

A Peculiar Case in the Middling Pressure Regime

The exception to several of the observations and conjectures in this regime is the recorded spectrum at 1.0×10^{-3} Torr, as seen in Figure 4.4. At this pressure, the slope after the peak shows no noticeable change until it reaches the detection limit, though it still does not match the simulated slope. According to the interpretation above, this suggests that there is no detection of the axial resonant frequency. Furthermore, while the resonant peak as seen in Figure 4.5 the simulated spectrum is taller and wider at the base than the recorded spectrum as for the other pressures in this regime, these observations are no longer explained solely by a larger damping coefficient. This is because the recorded resonant peak has a different shape; it has become asymmetric. While this asymmetry may have contributions from the noise peak at 168 Hz, this cannot be the sole cause. A possible interpretation of this asymmetry is that there are many peaks making up this broad peak. Physically, this would mean that we can detect multiple resonant frequencies at this pressure.

Another peculiarity at 1.0×10^{-3} Torr is that the spectrum does not have a change in slope around
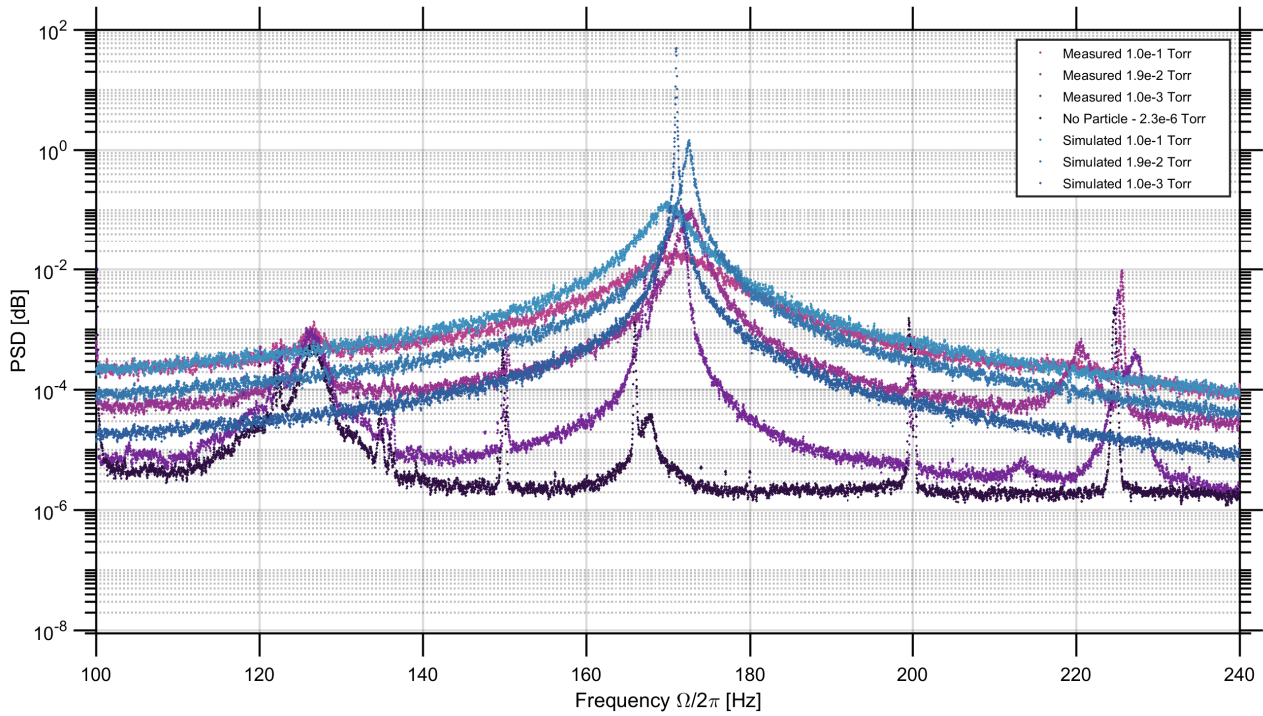
Figure 4.5: Power spectral density of middle pressure spectra, with measured and simulated data, focused on the resonant peaks.

900 Hz. This is the only pressure for which the PSD (from both cooled and non-cooled data sets) does not show the change in slope below 1.0×10^{-1} Torr. This may have been caused by the process of reaching this pressure, as described earlier. That is, the great length of time with the cooling on, and the possible change in the particle's environment from the raising of the pressure by two orders of magnitude has effected the particle's motion significantly. However, we see a peak at 340 Hz, where we expected the axial peak from the modelling chapter. There appears to be no contribution from this mode in this spectrum; the peaks around 500 Hz are harmonics of the line noise, the peak at 126 Hz, and the primary resonant peak at 170 Hz. However, the absence of a peak at the axial resonant frequency in this spectrum is not to say that the axial mode was unoccupied, just that it was unobserved for this measurement. It is possible that the detection system, which is designed to detect the horizontal motion of the trapped particle, simply did not produce a significant signal capturing the axial motion.

It is worth noting that the spectrum at this pressure is the closest in amplitude to the noise spectrum of the entire catalogue of measurements, so may well be the cleanest data recorded in the project. The parallel resonant peak around 220 Hz is still visible in this data, but the change in slope was attributed to the axial resonant frequency around 500 Hz. Further harmonics are identifiable in this spectrum, as

were identified earlier for the other pressures in this regime. The peak at 340 Hz could be interpreted as a harmonic of the main 170 Hz peak, but we have already stated above that this aligns with the predicted axial mode frequency, which is what it likely is.

4.2.3   The Lowest Pressures

The lowest pressure regime, seen in Figure 4.6, was defined by the violation of the expected trend for the amplitude of the baseline to continue decreasing with decreasing pressure. That our data shows the opposite is also perplexing because of our measurement system. When the pressure decreases, the damping coefficient decreases, allowing the particle to explore more of the trap. This increases the amplitude of the particle's motion, such that the entirety of the shadow of the particle is detected by only one photodetector. This results in a maximum value of the signal, such that no extra position data is collected other than that the particle is in a particular region. This reduction in position information should decrease the general amplitude of the PSD, while raising the amplitude of the harmonics of the resonant frequency. While the amplitudes of the third harmonics are raised compared to previous pressures, the baseline also rises.
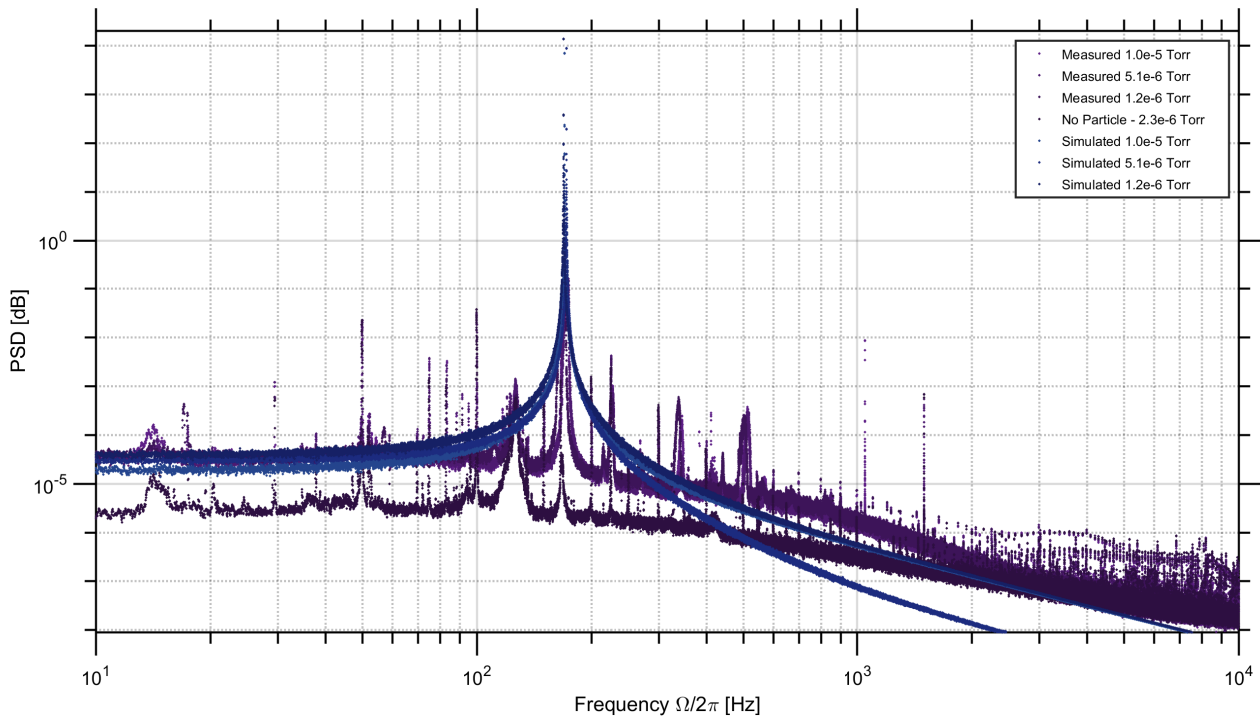

Figure 4.6: Power spectral density of the low pressure spectra, with measured and simulated data.

The peaks discussed for the previous regime are all present in Figures 4.6 and 4.7: the primary resonant peak at 170 Hz with second and third harmonics, the parallel resonant peak at 220 Hz and

its second harmonic, and various noise peaks. The change in slope around 900 Hz is present once more. We can also see contributions from the axial peak, which aligns with the second harmonic of the main resonant peak at these pressures.The trend of the primary resonant peaks in the simulation spectra being taller and wider at the base than the measured spectra has continued. Furthermore, the main resonant peaks of the measured spectra in this regime are wide and asymmetric, with the width increasing as the pressure decreases. This is a strong indicator that the trap is not a harmonic potential, as was originally thought, but an anharmonic potential.
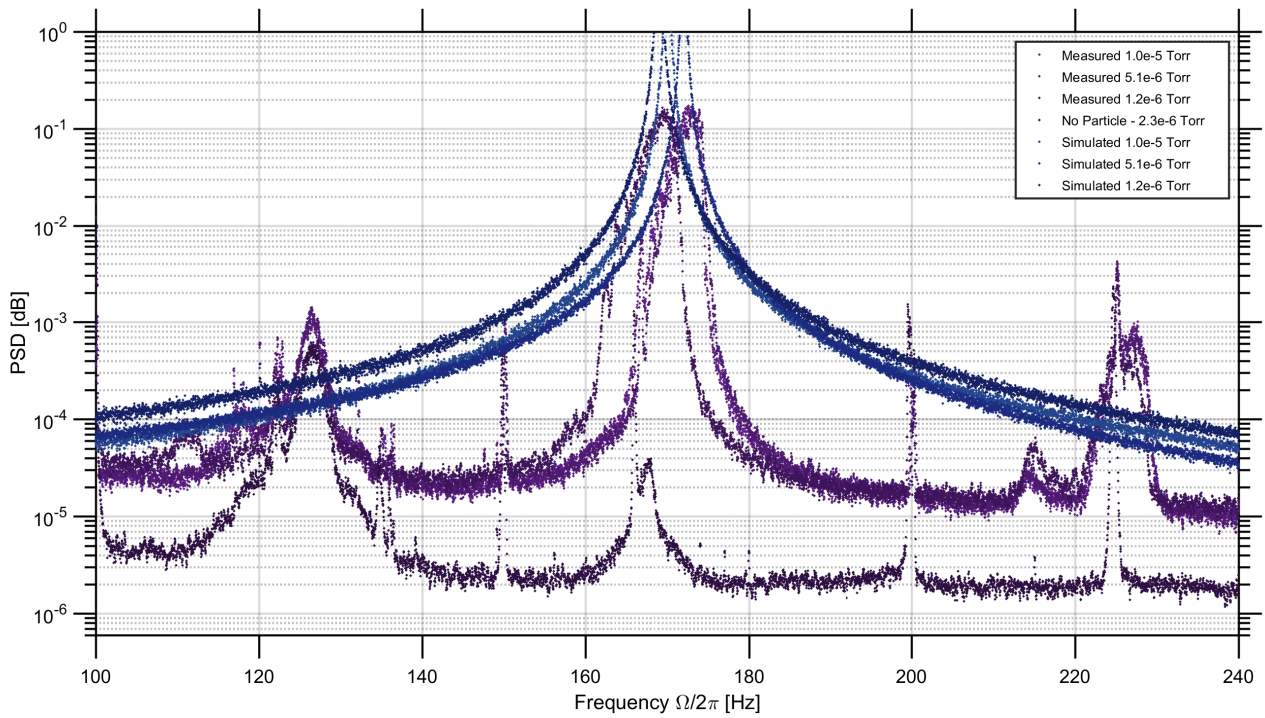

Figure 4.7: Power spectral density of the low pressure spectra, with measured and simulated data, focused on the resonant peaks.

An Anharmonic Potential?

To confirm the hypothesis that the trapping potential is anharmonic rather than harmonic, we expanded the region examined in the three dimensional magnetic modelling, seen in Figure 4.8. By expanding the square of the magnetic field (which is proportional to the trapping potential) into a Taylor series, we found that the quartic term had a non-trivial component. The ratio of the quartic and quadratic coefficients, λ, was used to simulate the potential again. The peak in the spectrum of this simulation looked similar to the broader, asymmetric peaks measured at 1.0×10^{-3} Torr and below, but the width did not quite match, as seen in Figure 4.9. With a λ a few orders of magnitude larger, a match in

width was found. This larger anharmonicity is likely caused by the non-ideal shape of the magnets, as discussed previously, together with the porosity, large grain size, and demagnetisation of the magnets. This larger value of λ also produced a peak at the third harmonic in the simulation spectra, which is seen in the measured spectra as well. However, we were unable to produce simulations that agreed well with the recorded peaks for all of the measured pressures which saw this anharmonicity. This was due to the varying nature of the resonant frequency, as changing this frequency in the simulation to match the recorded frequency produced a differently shaped peak. Indeed, merely changing the pressure in the simulation changed the shape of the peak in the simulation, sometimes quite drastically. Furthermore, as knowing the exact value of λ was of little importance, time was not spent trying to find better fits for all other relevant pressures.
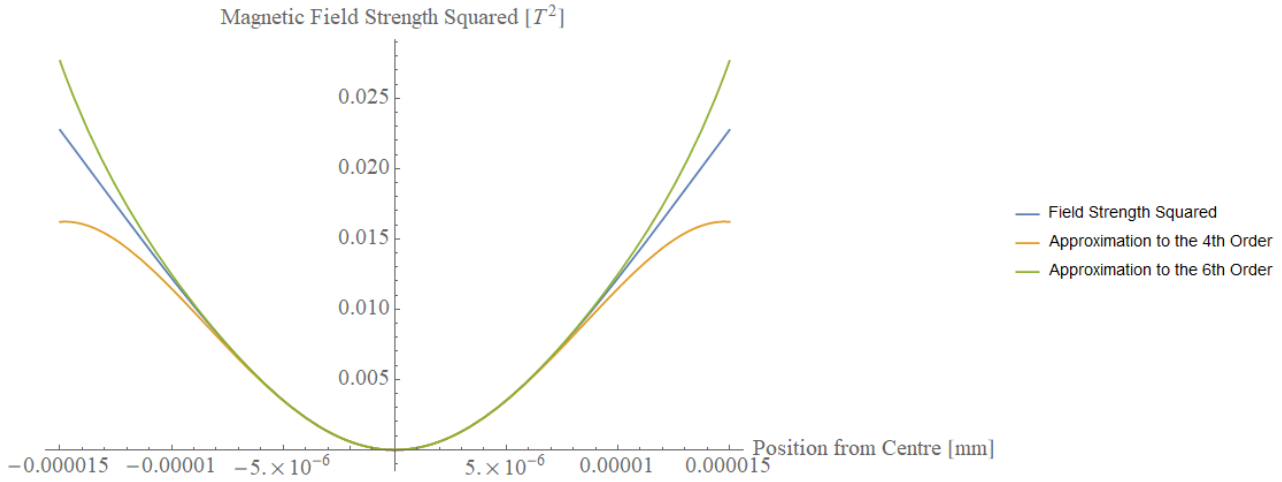

Figure 4.8: The magnetic field strength squared (y-axis, with units of T^2) in the radial dimension (x-axis, with units of mm) of the ideal magnetic trap from the three dimensional modelling (middle). Other plots show the 6th order Taylor series expansion (upper), and the 4th order Taylor series expansion (lower).

With this anharmonicity in mind, it is understood that at high pressures - the pressures above 1.0×10^{-3} Torr - the particle is confined to the harmonic parts of the trap due to the strong damping of the air, such that a single peak is observed, as was initially expected. However, for pressures at 1.0×10^{-3} Torr and below, the damping due to the air is weak enough that the particle can explore more of the trap. The parts of the trap further from the centre are more strongly anharmonic, such that harmonic theory can no longer account for the observed motion of the particle.

It should be noted that it is also likely that the cause of some of the amplitude of the widened peak and its harmonics is from the nonlinear detection system. However, this cannot account for all of the
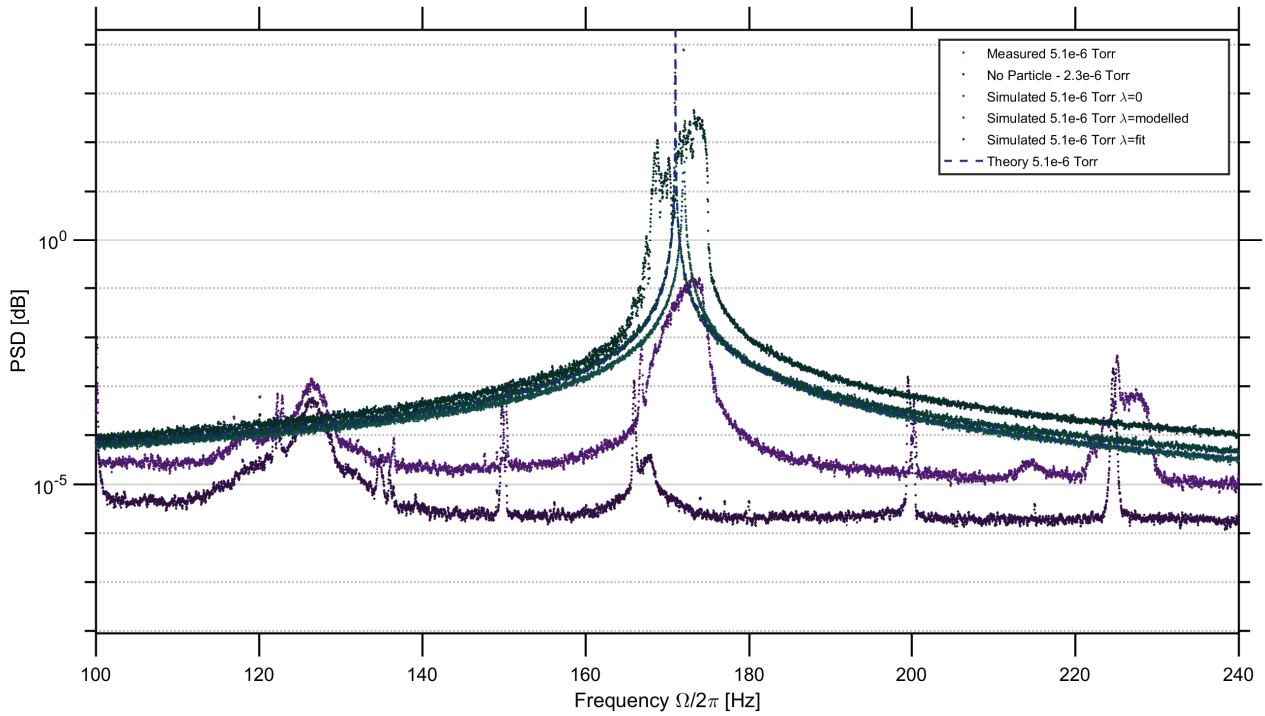
Figure 4.9: Power spectral density of measured, expected and simulated data at 5.1×10^{-6} Torr, around the resonant peaks. Simulations with different values of the quartic potential coefficient λ are displayed, simulating the harmonic potential, the ideal potential given by the magnetic modelling, and fitting the measured potential.

observed motion, especially as the particle is too strongly trapped at low pressures to be exploring a harmonic potential.

All in all, the recorded PSDs show some of the elements expected for the motion of a Brownian particle: the flat baseline before the peak, the peak itself (when the pressure is low enough), and the rolling away after the peak. While the slope of the latter does not agree with the expected slope from the one dimensional case, and the starting points of the roll off are also in disagreement, the presence of these features in a non-ideal, multidimensional system is an observation of Brownian motion.

4.3   Cooling

Our cooling system uses the differential of the measured signal to produce a magnetic field from a pair of Helmholtz coils. This cools the motion of the trapped particle in the measured dimension by effectively increasing the damping coefficient depending on the particle's position. The usual practice when measuring the position of a cooled, trapped particle is to cool the particle's motion until an

equilibrium point is reached, such that the energy removed by cooling is matched by the thermal noise in the system. After this equilibrium state is reached, the cooling is turned off, and data is recorded as the particle's motion slowly heats up. However, in our case, the time it takes for the particle to resume its motion is around 6 seconds, which is too short a time in which to take data by this method. This quick reheating indicates that there is coupling between the cooled dimension of motion and the other dimensions of motion of the particle. If this coupling were strong, and energy was still in one of the other dimensions of motion, then the energy could pass quickly into the transverse dimension of motion. However, if the coupling were strong, then cooling the particle's motion in the transverse dimension would mean energy could pass into that dimension from the other dimensions of motion, and so cool all dimensions, resulting in low energy in all dimensions of motion. The opposite is also true; if the coupling is weak, more energy can remain in the non-cooled dimensions of motion, but that energy would not return to the cooled dimension of motion quickly. Regardless of the strength of the coupling, we could not take data by the usual procedure. Instead, data was recorded while the cooling was on, for the same length of time and sampling frequency as outlined earlier.

Figure 4.10 shows that the PSDs for the lowest pressures, at which the cooling actually cooled the motion of the particle, are very similar to the PSDs which did not have cooling on at the same pressures, in Figures 4.4 and 4.6. Notable differences include the reduction of the main resonant peak and its harmonics to close to the baseline of each spectrum, and the increase in the amplitude of the peak around 125 Hz, the parallel resonant peak at 225 Hz and its second harmonic. The decrease of the main resonant peak shows the cooling has cooled the transverse motion at this frequency almost completely. However, the increase in amplitude of the parallel resonance peak suggests that the motion in the dimension parallel to the beam has increased. This may not be the case, as the increase could be due to increased sensitivity to other motion with the motion in the transverse dimension almost completely removed - that is, the decrease of the "signal" in the motion at the transverse resonant frequency has increased the effect of the "noise" of the motion at the parallel resonant frequency.

With these cooled PSDs, we can attempt to find the lowest temperature limit of this system. In previous work, it has been suggested that the cooling force in one dimension does not affect the velocity of the particle in another dimension, then the effective damping from the cooling, Γ_c can simply be added to the damping coefficient from the gas, Γ_0, to produce the total damping experienced by the particle, $\Gamma_{tot} = \Gamma_0 + \Gamma_c$ [17]. This total damping coefficient replaces Γ_0 in the formula for the expected spectrum. Additionally, the temperature of the gas T_0 can be replaced with the temperature limit with
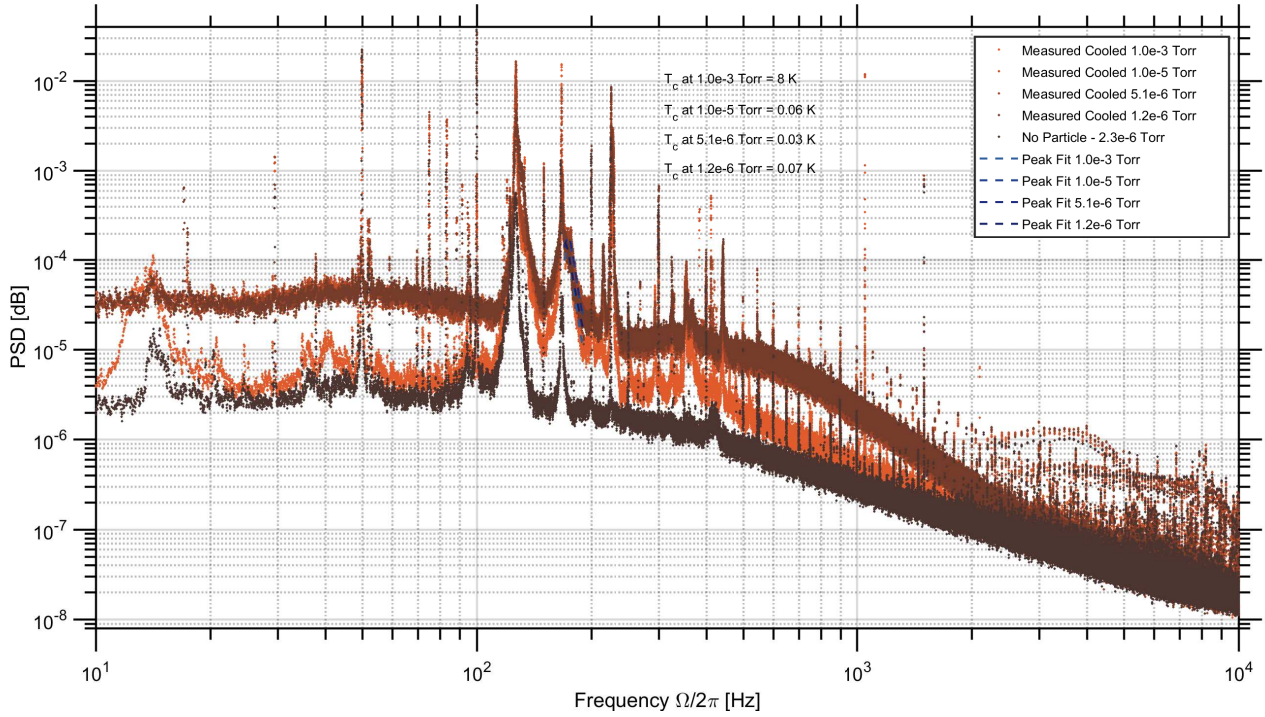
Figure 4.10: Power spectral density of all cooled measured data, with fits of $S_c(\Omega)$ on the peak at 170 Hz. The temperature is calculated from these fits, giving an indication of the lowest temperatures achievable with our system at each pressure.

the cooling on $T_c = T_0\Gamma_0/\Gamma_{tot}$, producing the equation

$$S_c(\Omega) = \frac{2k_B T_0\Gamma_0}{m} \frac{1}{(\omega_0^2 - \Omega^2)^2 + \Omega^2(\Gamma_0 + \Gamma_c)^2}. \tag{4.3}$$

By fitting this equation to the cooled PSDs, but being careful not to include data significantly affected by the noise peak at 167 Hz, the temperature at each recorded pressure could be calculated, as seen in Figure 4.11. A value for Γ_0 was required for this calculation, and so the values used were those calculated from the pressures measured. As discussed earlier, these values are not ideal for the data at these pressures because the particle spends a significant amount of time exploring the anharmonic regions of the trapping potential at these pressures. Equation 4.3 also considers a harmonic potential, when we have an anharmonic potential. However, as the motion of the particle has been cooled so heavily, we can approximate our potential to a harmonic potential, as the particle does not explore the anharmonic regions when cooled. Therefore, the concerns of whether the value of Γ_0 is accurate lie only with the measurement of the pressure in a confined space, and the difficulties associated with that outlined previously. As such, the calculated temperatures give a good indication of the level of cooling possible with our system, but should not be interpreted as accurate.
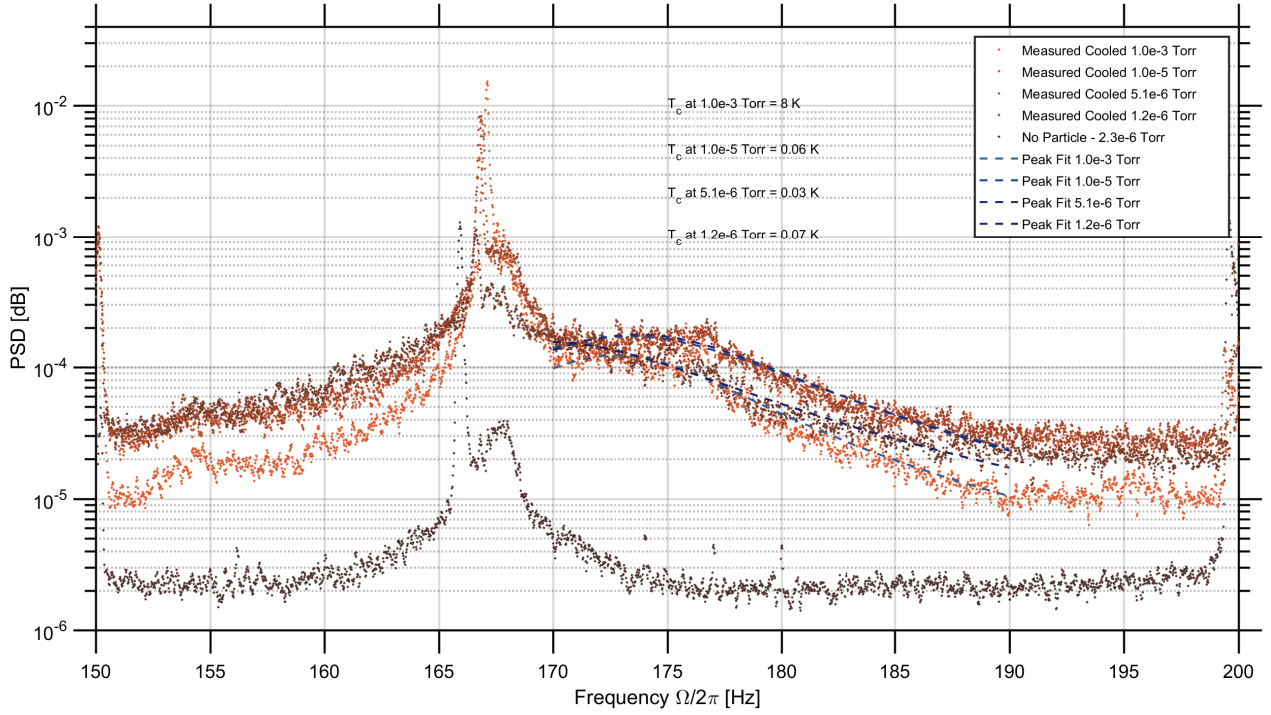
Figure 4.11: Power spectral density of all cooled measured data, with fits of $S_c(\Omega)$ on the peak at 170 Hz, which the view is focused around. The temperatures are calculated using the fits, which give an indication of the lowest temperatures achievable with our system at each pressure. The fits are for only about half the cooled resonant peak, because of the nearby noise peak.

4.4   MSDs

As the data we recorded is not a true position signal, but some nonlinear relation to the true position signal (limited when the amplitude of the motion is too large), the amplitude values, and units, of our MSDs only describe the mean square of the change in intensity of the optical signal. However, the MSDs are still useful, as they show the shape of the true MSDs, and so can be used to observe the Brownian motion of the trapped particle as the environment changes in pressure.

In previous work, the mean square displacement was used to show that Brownian motion was recorded in the ballistic regime, rather than the diffusive regime considered by Einstein [12]. These MSDs showed an increase at a rate proportional to t^2 at short time scales, and converged at long time scales to a constant dependent on the trapping frequency. In the intermediate time scale, the MSDs oscillated with an amplitude decaying in time. A similar behaviour is seen in our MSDs at higher pressures - those at 1.0×10^{-1} Torr or above, as seen in Figure 4.12. These MSDs match the shape of the previous work well [12]. However, at 1.0×10^{-3} Torr and below we see different behaviour. In

this regime, the amplitude of the troughs in the oscillation increase at a faster rate than the decrease of the amplitude of the peaks. This behaviour is expected by the equations for a harmonic trapping potential at low pressure. This is odd, as the PSDs show a clear departure from the expected values at the lowest pressures. The only departures from the expected results here are misalignment of the oscillations in time, which could be caused by the variation in resonant frequency, and the amplitude of the troughs. The measured troughs are much higher than the expected values, which could be due to the noise in the measurements, the limits of the detection system, and the inaccurate pressure readings. The noise is very high, and it is unclear how it influences the data in this analysis. The detection limit restricts the measurement range, which would result in smaller peak to peak amplitudes than expected. Finally, the pressure readings are used to calculate the damping coefficient used for the predictions; if the pressure in the trap is higher than what is measured, the damping coefficient would be higher, and the predictions would not match. To test whether an anharmonic potential can contribute to the observed disparities, we will compare the measured data with simulations and the prediction for a single pressure in Figure 4.13.
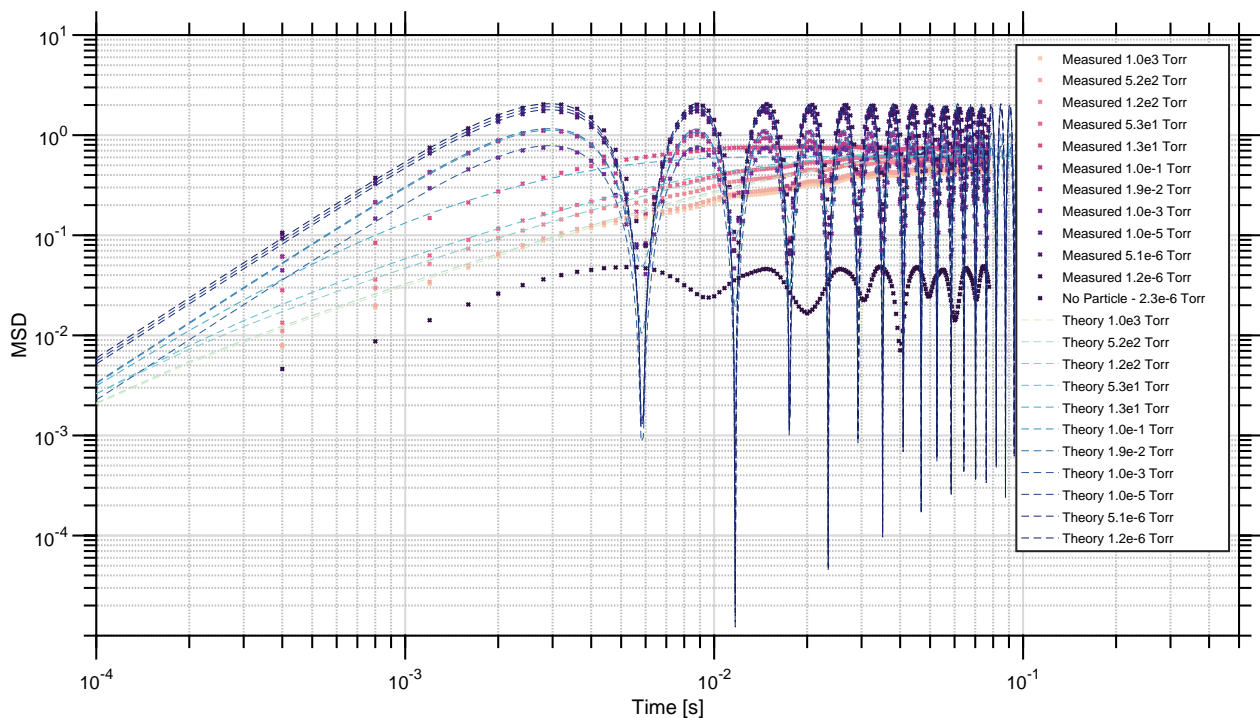

Figure 4.12: Mean square displacement of all non-cooled measured data, and expected results. The noise MSD is quite large, showing how noisy our system is.

Examining Figure 4.13 shows that nothing about the measured MSD is explained better by the anharmonic simulations than by the harmonic results. It seems odd that the anharmonic simulations

match the harmonic simulations so well. One might expect the period of the oscillations to change, as they seem dependent on the resonant frequency, and the measured and anharmonic simulated PSDs at this pressure had wider peaks, rather than well define harmonic frequencies. Instead, with the agreement of theory and all simulations, there is no argument for or against whether our trapping potential is harmonic or anharmonic, as the measured results fit the expected data quite well, showing that we have indeed observed Brownian motion at very low pressures.
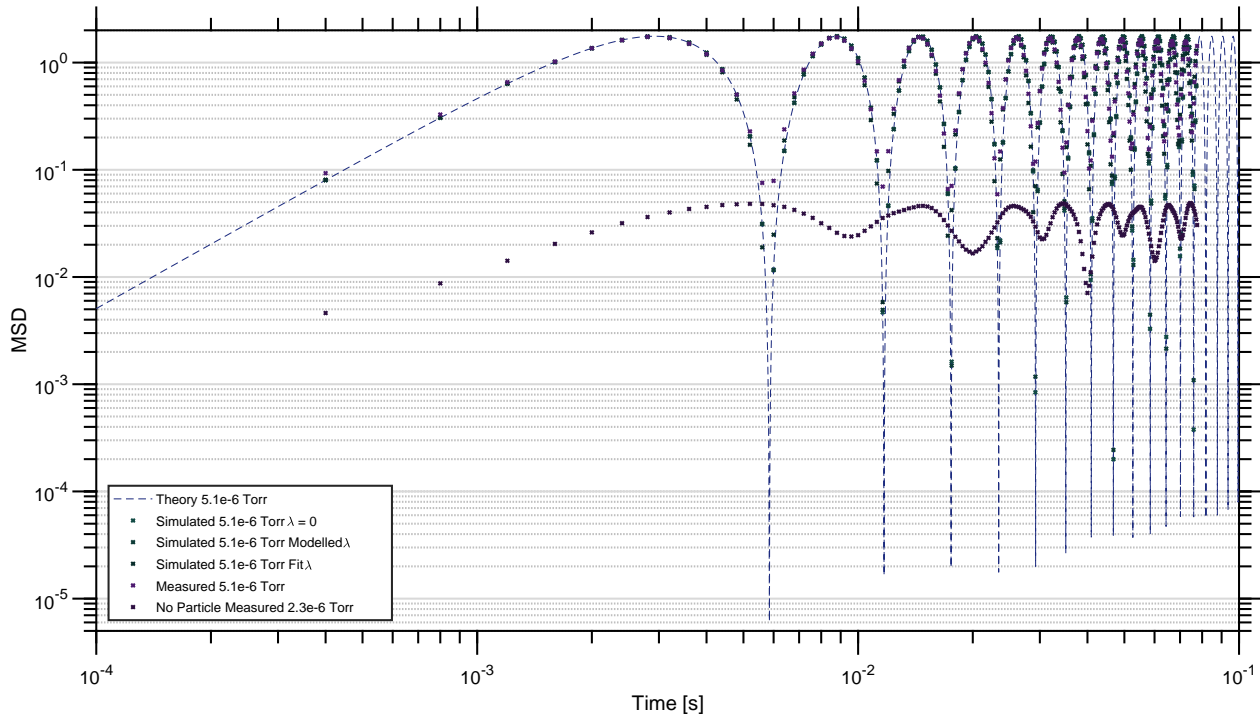

Figure 4.13: Mean square displacement of measured data at 5.1×10^{-6} Torr, expected results for a harmonic trap, and simulations for a harmonic potential, the anharmonic potential suggested by magnetic modelling, and the anharmonic potential found in Figure 4.9.

4.5 Velocity Measurements and Statistical Mechanics

In previous work, measurements of the instantaneous velocity of a Brownian particle at sub-atmospheric pressures were made to test statistical physics [12]. Observations of the Maxwell-Boltzmann velocity distribution, and experimental confirmation of the energy equipartition theorem were accomplished. We analysed our data in a similar fashion, shown in Figure 4.14, using the difference between consecutive data values and the change in time between those measurements to produce an instantaneous velocity signal.
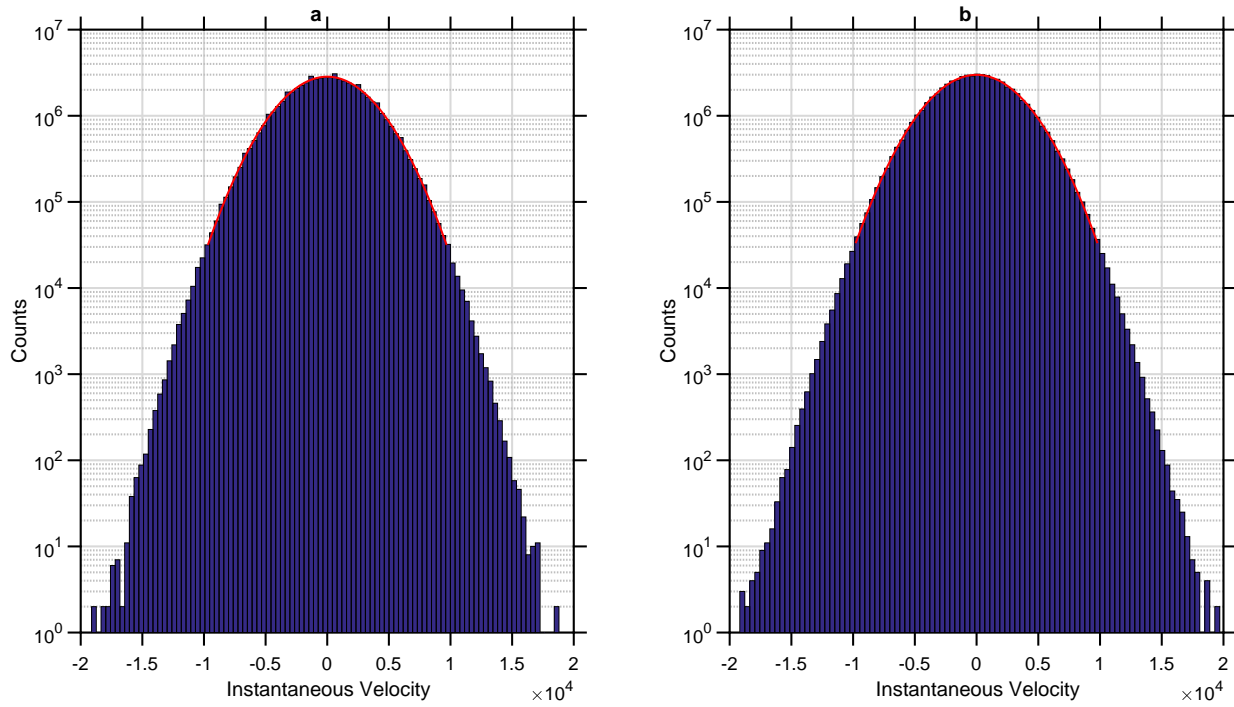
Figure 4.14: Instantaneous velocity distribution histograms, calculated by finite difference of the measured data. Both plots match normal distributions, with approximately equal means and standard deviations. a) The velocity distribution of the lowest pressure measured, 1.2×10^{-6} Torr. b) The velocity distribution of the noise data.

We can see that our velocity distributions have a normal distribution, matching the Maxwell-Boltzmann velocity distribution. However, we must also consider the noise in the measurement system, given by the velocity distribution of the data taken with no particle in the trap. This shows a distribution with the same range and amplitude as the measured data. This indicates that there is too much noise in our measurement system to create usable velocity data. As such, we cannot test the energy equipartition theorem, as any calculated root mean square velocity would be so noisy as to be meaningless.

On the other hand, considering that our measured data is not a true position signal, this velocity distribution would not have had the meaning we were to ascribe to it. What we have produced in Figure 4.14 is the distribution of the change in the intensity of light. These distributions have a nonlinear relation to the position data of the particle. Therefore, the finite difference of our signal will not give a true instantaneous velocity signal.

5

Conclusion

With the results presented and discussed, this chapter will look to summarise this project, and its place in the broader field of research. This will entail: a summary of the ultimate goals of the project in the broader field of research, which are to create and sustain a macroscopic quantum superposition of states and to build precision sensing technology; the goals of this project, which are to observe Brownian motion at low pressures, test the energy equipartition theorem at low pressures, and characterise a novel, passive, magnetic trap; and the progress made towards these goals by this project. We will finish by outlining areas of the system which should be improved to reach the ultimate goals of the broader field of research, and the applications and implications this project has on the broader field of research.

5.1   Project Summary

This section will summarise the goals of the broader field of research, the goals of this project, and how we worked towards those goals.

In this project, we set out to design and build a passive magnetic trap which could trap diamond micro-particles. The ultimate goals of this trap would be to create a macroscopic quantum superposition of states (or cat state) with the trapped micro-particle, and to create an harmonic oscillator of high quality to enable precision inertial and electromagnetic measurement. In order to reach the former goal, the trap must be engineered such that the trapped particle will have a very low rate of energy loss. In our setup, this means very low pressures must be reached with the particle remaining trapped. It also requires our trap to have a harmonic potential with a high resonant frequency. The observation of Brownian motion in the ballistic regime and the test of the energy equipartition theorem also require these conditions, but to a lesser extent. As such, observing the Brownian motion and testing the equipartition theorem at lower pressures than before is a fine test of the capabilities of our trap.

In order to design our trap to keep a particle trapped at low pressures and have a high resonant frequency, we used magnetic field modelling to optimise the design of the magnets. We simulated the position data of a diamond micro-particle trapped by this ideal magnetic trapping configuration for various pressures, with thermal noise to reproduce Brownian motion. This gave promising results, so the challenging task of shaping the magnets was undertaken. Once magnets were sufficiently shaped, the trap was made and mounted in the vacuum chamber. A cooling system was also constructed of Helmholtz coils, to use a direct feedback cooling signal to cool the motion of the trapped particle. Cooling the particle's motion was expected to be necessary for the particle to remain trapped at lower pressures. A cooling system would also be necessary for the cooling of the particle's motion to achieve a cat state.

Therefore, the aims of this project were to design and build a passive magnetic trap, trap a diamond micro-particle, keep it trapped at very low pressures, characterise the shape and strength of the trap, observe Brownian motion for the pressure range covered, determine the effectiveness of the cooling system, and test the energy equipartition theorem at low pressures. Achieving these goals will be major progress towards the goals of the broader field of research of the creation of a cat state, and precision inertial and electromagnetic measurement technology.

5.2   Our Progress to Our Goals

In this section we will summarise the progress we have made toward the project goals, and toward the ultimate goals outlined above.

We were successful in building a purely magnetic trap, capable of trapping diamond micro-particles at the lowest pressures our vacuum system reached, which was 1×10^{-6} Torr. Furthermore, once a particle was trapped and the pressure lowered, the particle would remain trapped indefinitely without assistance from the cooling system. This long-term passive trapping was achieved at these pressures by the unexpected shape of the trapping potential. We expected the potential to be harmonic, which it is (approximately) around the centre of the trap, but the further the particle went from the centre of the trap, the more the anharmonic potential affected it. This anharmonicity produced a much stronger trapping force the further the particle went from the centre, preventing the particle from escaping the trap at low pressures. This anharmonicity was also seen when examining the Power Spectrum Density (PSD) plots at low pressures, and was predicted by the magnetic modelling once we expanded the region of evaluation of the potential. With this finding, the simulations at low pressure were adjusted accordingly to better reflect the nature of the motion the trapped particle undergoes in our trap at low pressure. However, the anharmonicity of the potential of our trap was found to be larger than what was modelled. This disparity is likely due to the physical differences of our trap to the ideal trap that was modelled. These differences include: the physical shape of the magnet tips, which were supposed to be sharp square pyramids, but ended up with more of a wedge shape, with a blunt tip; the larger grain size of the magnetic material, which changed the shape of the tips; and demagnetisation of the tips from close proximity to like poles, which the modelling software does not account for.

The anharmonic potential therefore allows the observation of Brownian motion at very low pressures at room temperature. The Brownian motion was seen in the PSDs and Mean Square Displacements (MSDs), where the experimental and simulated data mostly agree with the theory. The general shape of the PSDs at higher pressures where no anharmonic potential is observed match the theory for the Brownian motion well. This includes: the flat baseline, the peak around the resonant frequency the magnetic modelling predicted, and the roll-off of the power of the frequencies above the resonant frequency. Now, the theory is for Brownian motion in one dimension. However, as our trap is not ideal, and because of our detection system, we observe Brownian motion from two dimensions, and effects of the third dimension. This is likely the reason why the slopes of the roll-off do not match. The PSDs also help to characterise the trap, as we find the resonant frequency for the mode transverse to the beam line to be 170 Hz, and the mode parallel to the beam line to be 225 Hz. We cannot determine the frequency of the vertical mode, as there is not enough power in the signal to produce a clear peak. Note that the shapes of the peaks do not quite match exactly, likely due to some difference in the calculated damping coefficient to the real damping coefficient. This difference can be explained

by the large uncertainty is measuring the pressure, and the higher than measured pressure of the confined region of the trap. Fitting the theory to the experimental PSDs would likely give a much higher damping coefficient than the one measured, and the confined region having a higher pressure explains that.

At the lowest pressures, at 1.0×10^{-3} Torr and below, the anharmonic potential is evident in the widening of the resonant peak, and the change in shape to an asymmetric peak. At these pressures, the experimental data does not match the harmonic theory. An anharmonic simulation at 5.1×10^{-6} Torr agrees with the width of the peak of the experimental PSD for the same pressure, suggesting that the discrepancies with the theory at these lowest pressures is due to the particle exploring more of the anharmonic potential. The MSDs match the theory for the Brownian motion almost exactly (after scaling), with only the noise in the system, and the measurement of the pressure in the trapping region limiting the agreement. The agreement is in the slope at short time scales, the decaying oscillations at intermediate time scales, and the convergence to a constant at long time scales. It is surprising that the anharmonicity does not affect the MSD as much as it did the PSD, though this may be due to the noise and sampling rate of the detection system and simulations.

The anharmonic potential of the trap not only keeps the particle trapped at low pressures, but also increases the damping acting on the particle, increasing the rate at which the particle loses energy. This is detrimental to the ultimate goal of a harmonic oscillator with high mechanical quality for quantum and sensing applications. At least, it would be if the particle were allowed to explore the regions of the trap where the potential is more strongly anharmonic. Using cooling, we can keep the particle near the centre of the trap, such that the particle will experience an approximately harmonic potential. The evaluation of the data recorded with the cooling on found that the motion of the cooled mode could be cooled to the order of tens of milli-Kelvin with the current system. However, the time it takes for the particle to reach thermal equilibrium after the cooling is switched off is around 6 seconds. This must be due to mechanical noise shaking the magnets and injecting energy into the system. Therefore, the current system, with the noise and the current temperature limit, is unsuitable for conducting experiments to create a cat state.

The noise that injects energy into the system, thermalising the cooled particle so quickly, also hindered our testing of the the energy equipartition theorem. The instantaneous velocity distributions shown in the previous chapter showed almost identical trends for the experimental data from the lowest pressure and the experimental data for the trap with no particle in it, which gives a measure for the noise in the system. As such, any calculation of the root mean square velocity would have

enormous uncertainty. It is also worth noting that as our detection system produces data which is nonlinearly related to the signal of the position of the trapped particle, the finite difference method used to determine the instantaneous velocity of our signal did not give the instantaneous velocity of the particle.

In summary, our project did not meet all the project goals, as it failed to test the energy equipartition theorem due to the amount of noise in our system. However, the project succeeded in observing Brownian motion at low pressures, and partly succeeded in characterising the magnetic trap. In order to fully characterise the trap, the resonant frequencies in all directions must be identified, and we are lacking the resonant frequency of the vertical mode. The cooling system proved very effective, though the noise in the system heated the motion of the cooled particle much too quickly for this system to be used to create a cat state as it is.

5.3   Future Work and Applications

The progress made in this project toward the ultimate goals of a system capable of the creation of a cat state, and improving sensing technology has been mixed. The effectiveness of the current system has been evaluated; now the areas that need improving to reach the ultimate goals for the broader field of research, and for the project, will be identified. The future work needed to reach the ultimate goals, and the future applications of this research will also be discussed.

The project shows that the current setup is not yet ready for the creation and measurement of a cat state. This is partly because the system not only has to be a platform capable of creating such a state, but also must be able to maintain that state for a long enough period of time to enable operations upon that state. As mentioned above, there is significant noise in the system, such that the particle heats up from a cooled temperature in roughly 6 seconds. To extend the coherence time requires minimising this noise. This noise comes from a variety of sources. One such source is the turbo vacuum pump, which shakes the entire vacuum chamber at 1050 Hz when in standby mode, and at 1500 Hz when at full speed. This noise source can be removed by installing an ion vacuum pump. The ion pump will enable much lower pressures than the turbo pump, and allows the turbo pump to be switched off, removing it as a source of noise. As the ion pump has no moving parts, and no outlet, it will not cause mechanical noise. The large voltages that ionise and embed the gas particles in a block of tantalum produce a large magnetic field, but magnetic shielding can be used to preserve the trapping potential. Therefore, not only would we be able to remove noise from the system, but we would be able to

reach much lower pressures, further lowering the cooling limit of the system. However, to reach these low pressures with this pump would also require a higher quality vacuum chamber. This should also provide an environment which is more isolated from the mechanical vibrations which pass through the optical table. An improved floating optical table could also reduce mechanical noise influencing the particle from other sources in the laboratory.

In addition to the mechanical noise influencing the particle, we have electrical noise interfering with our signal. This affects the measurements from the signal, as well as the cooling signal, and so affects the effectiveness of the cooling. Noise peaks from the room lights being used by other lab users, from the electrical mains lines, and from the refresh rate from the computer monitors are littered throughout our experimental PSDs, but there is little that can be done about this other than improved light shielding around the apparatus. Other sources of electrical noise occur in the detection of the optical signal by the photodiodes, the filtering and amplification of this signal by the preamplifier, and in the digitising of the signal by the oscilloscope, all limiting the signal in some way. These noise sources can be reduced by upgrading the equipment. However, improving the dynamic range with a different digital oscilloscope would likely sacrifice some of the stability of the time base, and the stability of the time base is what gives the certainty in producing accurate frequency measurements. As such, the current digital oscilloscope is likely the best option, such that 72 dB is the best dynamic range we are likely to get. These improvements should allow for the testing of the energy equipartition theorem at low pressures. As mentioned, the noise in the measured signal also affects the cooling signal. Furthermore, the cooling signal receives additional noise from the power amplifier. Therefore, using a power amplifier with a higher signal-to-noise ratio would improve the transmission of a cleaner cooling signal, providing more effective cooling. Effective cooling means that cooling to the ground state, required for creating a cat state, is more achievable.

To probe the created cat state, the quantum system will need a handle. With the capability to trap diamond micro-particles, the ideal handle would be the spin states of a nitrogen vacancy (NV) centre, or some other colour centre. However, due to the build up of static charge, we needed to coat our diamond particles in an anti-static agent to trap them. This coating would be detrimental to the probing of an NV centre's spin state, and would cause noise in a quantum measurement. As such, the trap mounting design will need to be improved to prevent the build up of static charge, such that coating the diamond particles is unnecessary. Indeed, engineering a new method to launch the diamond particles into the trap may be required, as the current method of directing the particles with a stream of gas is the apparent cause of the static charge. A piezoelectric launcher could prove to

remove this issue, and would allow for the launching of smaller diamond particles. On the other hand, smaller particles are likely to be harder to trap, and keep trapped, requiring a stronger trap. It would also be much harder to trap single particles, and the motion of two or more trapped particles is likely to be much more complicated. Thus designing a novel launching method could prove an invaluable step towards creating a cat state with this trap.

It was found that the magnet tips were not quite the desired shape. The desired shape of the tips was a square pyramid, with a $28.75°$ angle of ascension between each face and the base of the pyramid, with the faces coming together to form a sharp point. However, due to the large grain size of the magnet, the resulting tips were more wedge shaped. This is because that while the tip was being faceted, the large grain size caused the point to fracture. As such, the closest shape possible was a wedge, where one pair of opposite faces did not quite meet, thus avoiding fracturing, but forming a ridge rather than a point. The production of a sharper tip would not only require faceting with greater finesse, but also a magnetic material with a finer grain size, so that the length of the ridge would be smaller. This will allow a more pointed tip to be faceted, increasing the symmetry of the magnet and the magnetic field, bringing the design closer to the ideal shape. This would cause the second horizontal resonant frequency to approach equality with the first, such that only one horizontal and one vertical resonant frequency are found. A quadrant photodiode could then be used to find the resonant frequency in both directions simultaneously, in place of the current detection system.

A necessary improvement to this system is in the analysis of the optical signals. As has been mentioned, the measured signal is nonlinearly related to the position of the particle because the experimental measurement depends on movement of the cross-section of the particle over a dividing line. If the shape of the particle were approximated to a sphere, then a mathematical transformation could be applied to the signal to provide a truer measurement of the particle's position. However, as diamond crystals are not spherical, and the size and shape of the shadow changes as the particle rotates and moves parallel to the beamline, this may not improve the analysis of the experimental data markedly.

Further progress with this project could be made with more in-depth theoretical predictions and simulations. The effect from other modes aside from the one we were focusing on were evident in the PSDs, such that the one dimensional simulations did not quite match. If three dimensional simulations of the harmonic and anharmonic potentials were accomplished, then a more informed analysis of the experimental measurements could be made.

Despite the improvements that can be made to this system, this research has current applications.

For instance, in inertial sensing technology. While the trapped particle may heat up quickly after the cooling is switched off, it is cooled quite effectively when the cooling is on. However, the active cooling of the particle's motion is not the only use for this signal. The cooling signal provides information about the instantaneous velocity of the particle, and our detection system provides very precise measurement of the movement of the particle, down to sub-microns, and with a stable and fine time step of 10 μs. This provides information for the instantaneous velocity with high precision, which is exactly what an inertial sensor provides. Together with the magnetic trap being a passive trap, and the anharmonic potential keeping the particle trapped seemingly indefinitely at low pressures, this system is a great candidate for becoming an inertial sensor. Miniaturisation of the system for integration into electronics is possible, as no bulky and power consuming components are necessary, unlike optical traps. Integrating a magnetic trap into electronics would require magnetic shielding, to protect the trap and the electronics from interference, but this should be simple enough.

While this system is not yet ready to create and sustain cat states, the anharmonic potential does not disqualify the magnetic trap design from the possibility to create them in the future. Although a cat state requires a harmonic potential, and an anharmonic potential introduces unnecessary damping, a cat state must also be cooled substantially. As has already been mentioned, a particle with a low motional temperature will only explore the region around the trap centre, and the potential of this region in our trap is approximately harmonic. If the improvements discussed above - reducing the noise in the system, removing the need for the anti-static coating on the diamond micro-particles, and reducing the minimum achievable pressure - are made, then the trap should be capable of creating and sustaining cat states. This reduction in noise will result in the particle's motion taking a much longer time to heat up after being cooled. Therefore, the trap will have the potential to create and sustain cat states. The only limiting factor for this will be if enough noise can be removed from the system so that the coherence time of the cat state is long enough for the necessary operations to be performed on that state.

This project has exciting prospects. As we have discussed, there are many improvements to be made, such as those to reduce the noise in the system, to lower the pressure further, and to simplify the shape of the trapping potential. However, the progress made in this project towards cooling to the ground state, and in producing a system with the potential to be integrated into electronic devices as an inertial sensor is noteworthy. If more work is done in improving this system, it may not be long before a macroscopic quantum superposition of states is created.

List of Symbols

$\sqrt{\langle [\Delta x_{\mathrm{dif}}(t)]^2 \rangle}$ is the root mean square displacement of a Brownian particle in the diffusive regime

$\Delta x_{\mathrm{dif}}(t)$ . . . . . . is the displacement of a particle in the diffusive regime

D . . . . is the diffusion coefficient

k_B . . . . is the Boltzmann constant

T . . . . is the temperature of the fluid

γ . . . . is the Stokes friction coefficient

t . . . . is time

τ_p . . . . is the momentum stopping time

m . . . . is the mass of the Brownian particle

γ . . . . is the Stokes friction coefficient of the fluid environment

$\langle [\Delta x_{\mathrm{dif}}(t)]^2 \rangle$. is Einstein's diffusive mean square displacement

$\langle [\Delta x_{\mathrm{bal}}(t)]^2 \rangle$. is the ballistic mean square displacement

$\Delta x_{\mathrm{bal}}(t)$ . . . . . is the displacement of a particle in the ballistic regime

$f(v)$ . . . . is the normalised Maxwell-Boltzmann distribution

v . . . . is the instantaneous velocity of the Brownian particle

$\langle [\Delta x_{\mathrm{tra}}(t)]^2 \rangle$. is the MSD of a trapped Brownian particle, at low pressures

$\Delta x_{\text{tra}}(t)$ ...... is the displacement of a trapped particle in the ballistic regime

ω_0 .... is the resonant angular frequency of the trap

$\omega_1 = \sqrt{\omega_0^2 - \frac{1}{2\tau_p}^2}$

F_{mag} .... is the magnetic force on a diamagnet

χ .... is the magnetic susceptibility of the particle

V .... is the volume of the particle

μ_0 .... is the permeability of free space

$B = (\mathbf{B} \bullet \mathbf{B})^{1/2}$ is the magnitude of the magnetic field vector $\mathbf{B}$

$Q_{\text{mech}} = \omega_j/\Gamma_0$ is the mechanical quality factor

ω_j .... is the angular resonant frequency in the j dimension

Γ_0 .... is the damping coefficient

U_{mag} .... is potential due to magnetic field

χ_{gra} .... is the magnetic susceptibility of graphite

ρ_{gra} .... is the mass density of graphite

$a = -kx/m = \omega_0^2 x$ is the acceleration on of a harmonic oscillator

k .... is the spring constant

x .... is the position of the oscillator

ν .... is the linear frequency of the oscillator

χ_{dia} .... is the magnetic susceptibility of diamond

ρ_{dia} .... is the mass density of diamond

U_{tot} .... is the trapping potential

g .... is the acceleration due to gravity

$\tilde{x} = x + G \ldots$

A, C and G .. are constants

$K_n = l/r$ .... is the Knudsen number

l . . . . is the mean free path of the gas molecules

$c_K = \frac{0.31 K_n}{0.785 + 1.152 K_n + K_n^2}$

d . . . . diameter

p . . . . pressure

r . . . . is the radius of the trapped diamond microparticle

η . . . . is the viscosity coefficient of air

x . . . . is the position of the particle

ζ_n . . . . is Wiener noise

$x(t = 0) = 0, \frac{dx}{dt}|_{t=0} = 0$

$S(\Omega)$ . . . . is the power spectral density for Brownian particle in a harmonic trap

Ω . . . . is angular frequency

$\tau_p = 1/\Gamma_0$ . . . is the momentum relaxation time

$D = \frac{k_B T}{\Gamma_0 m}$ . . . . . is the diffusion coefficient

λ . . . . is the ratio of the quartic and quadratic coefficients

Γ_c . . . . is the effective damping from the cooling

$\Gamma_{tot} = \Gamma_0 + \Gamma_c$ is the total damping experienced by the particle when the cooling is on

T_0 . . . . is the temperature of the gas

$T_c = T_0 \Gamma_0 / \Gamma_{tot}$ is the temperature limit with the cooling on

$S_c(\Omega)$ . . . . is the power spectral density with cooling on

References

[1] R. Brown. *A brief account of microscopical observations made in the months of june, july and august, 1827, on the particles contained in the pollen of plants; and on the general existence of active molecules in organic and inorganic bodies.* Self-published Pamphlet .

[2] R. Brown. *The miscellaneous botanical words of Robert Brown: Volume 1* (R. Hardwicke, London, 1866).

[3] A. Einstein. *Über die von der molekularkinetischen theorie der wärme geforderte bewegung von in ruhenden flüssigkeiten suspendierten teilchen.* Annalen der Physik **322**(8), 549 (1905).

[4] A. Einstein. *Investigations on the Theory of the Brownian Movement* (Methuen & Co. Ltd., London, 1926).

[5] J. Bernstein. *Einstein and the existence of atoms.* American Journal of Physics **74**(10), 863 (2006).

[6] J. Perrin. *Mouvement brownien et réalité moléculaire.* Annales de Chimie et de Physique **8** (1909).

[7] J. Perrin. *Brownian Movement and Molecular Reality* (Taylor and Francis, London, 1910).

[8] A. Einstein. *Theoretische bemerkungen über die brownsche bewegung.* Zeit. f. Elektrochemie **13**, 41 (1907).

[9] A. Ashkin, J. M. Dziedzic, J. E. Bjorkholm, and S. Chu. *Observation of a single-beam gradient force optical trap for dielectric particles.* Optics Letters **11**(5), 288 (1986).

[10] K. C. Neuman and S. M. Block. *Optical trapping.* Review of Scientific Instruments **75**(9), 2787 (2004).

[11] K. Dholakia and W. M. Lee. *Optical trapping takes shape: The use of structured light fields.* Advances In Atomic, Molecular, and Optical Physics **56**, 261 (2008).

[12] T. Li, S. Kheifets, D. Medellin, and M. G. Raizen. *Measurement of the instantaneous velocity of a brownian particle.* Science **328**(5986), 1673 (2010).

[13] M. C. Wang and G. E. Uhlenbeck. *On the theory of the brownian motion ii.* Rev. Mod. Phys. **17**, 323 (1945).

[14] M. Aspelmeyer, T. J. Kippenberg, and F. Marquardt. *Cavity optomechanics.* Reviews of Modern Physics **86**(4), 1391 (2014).

[15] T. J. Kippenberg and K. J. Vahala. *Cavity optomechanics: Back-action at the mesoscale.* Science

321(5893), 1172 (2008).

[16] S. Singh, G. A. Phelps, D. S. Goldbaum, E. M. Wright, and P. Meystre. *All-optical optomechanics: An optical spring mirror*. Physical Review Letters **105**(21), 213602 (2010).

[17] T. Li, S. Kheifets, and M. G. Raizen. *Millikelvin cooling of an optically trapped microsphere in vacuum*. Nat Phys **7**(7), 527 (2011).

[18] Z.-q. Yin, T. Li, X. Zhang, and L. M. Duan. *Large quantum superpositions of a levitated nanodiamond through spin-optomechanical coupling*. Physical Review A **88**(3), 033614 (2013).

[19] A. T. M. A. Rahman, A. C. Frangeskou, M. S. Kim, S. Bose, G. W. Morley, and P. F. Barker. *Burning and graphitization of optically levitated nanodiamonds in vacuum*. Sci Rep **6**, 21633 (2016).

[20] J.-F. Hsu, P. Ji, C. W. Lewandowski, and B. D'Urso. *Cooling the motion of diamond nanocrystals in a magneto-gravitational trap in high vacuum*. Sci Rep **6**, 30125 (2016).

[21] M. D. Simon and A. K. Geim. *Diamagnetic levitation: Flying frogs and floating magnets (invited)*. Journal of Applied Physics **87**(9), 6200 (2000).

[22] R. S. M. Rikken, R. J. M. Nolte, J. C. Maan, J. C. M. van Hest, D. A. Wilson, and P. C. M. Christianen. *Manipulation of micro- and nanostructure motion with magnetic fields*. Soft Matter **10**, 1295 (2014).

[23] G. D. Pasquale, S. Iamoni, and A. Somà. *3d numerical modeling and experimental validation of diamagnetic levitating suspension in the static field*. International Journal of Mechanical Sciences **68**(Supplement C), 56 (2013).

[24] O. Chubar, P. Elleaume, and J. Chavanne. *A three-dimensional magnetostatics computer code for insertion devices* **5**, 481 (1998).

[25] J. Heremans, C. H. Olk, and D. T. Morelli. *Magnetic susceptibility of carbon structures*. Phys. Rev. B **49**, 15122 (1994).

[26] A. F. Ismail, K. Khulbe, and T. Matsuura. *Gas separation membranes: Polymeric and inorganic*. Springer p. 14 (2015).

[27] K. E. Spear and J. P. Dismukes. *Synthetic diamond - emerging cvd science and technology*. Wiley (1994).

[28] D. R. Lide. *Crc handbook of chemistry and physics*. CRC Press (2005).

[29] G. R. Dennis, J. J. Hope, and M. T. Johnsson. *Xmds2: Fast, scalable simulation of coupled stochastic partial differential equations*. Computer Physics Communications **184**(1), 201 (2013).

[30] S. Zhang. *Finding the right color palettes for data visualizations* (2017). URL https://blog.graphiq.com/finding-the-right-color-palettes-for-data-visualizations-fcd4e707a283.